To cite this version :

Non-operable glioblastoma IDH wild type: proposition of a patient-specific forecasting by imaging-informed poromechanical modeling

Stéphane Urcun[1,2,3], Davide Baroli[4,5], Pierre-Yves Rohan[2], Wafa Skalli[2], Vincent Lubrano[6], Stéphane P.A. Bordas[1], and Giuseppe Sciumè[*3]

[1]Institute for Computational Engineering Sciences, Department of Engineering Sciences, Faculté des Sciences, de la Technologie et de Médecine, Université du Luxembourg, Campus Kirchberg, Luxembourg
[2]Institut de Biomécanique Humaine Georges Charpak, Paris
[3]Université de Bordeaux
[4]Università della Svizzera Italiana, Euler Institute, Lugano
[5]Aachen Institute for Advanced Study in Computational Engineering Science, Rheinisch-Westfälische Technische Hochschule Aachen, Aachen
[6]Hôpital Pierre-Paul Riquet, Toulouse

December 29, 2021

Abstract

Introduction

In global cancer statistics, primary brain tumor has the 21th rank of incidence but reach the 14th rank of mortality [1]. Glioma represent the large majority of malignant primary brain tumor. The group of diffuse glioma, 'diffuse' being opposed to 'circumscribed', is the one with the worst prognosis. The diagnosis of diffuse glioma was first based histological features as infiltrative glioma cells along pre-existing tissue elements, historically known as secondary Scherer's structures. The staging of diffuse glioma is based on specific and cumulative histological features: nuclear atypia for stage II, mitotic activity for stage III denoted anaplasic, necrosis and/or microvascular proliferation for stage IV, denoted glioblastoma multiforme (GBM). This study is interested on the highest WHO grade of glioma, grade IV GBM. This stage has the poorest prognosis with a median survival around 15 months, and a 5-year survival rate at 5.8%, constant since the year 2000 [2]. The update of the World Health Organisation (WHO) classification in 2016 [3], which includes molecular biomarkers, now differentiates the diffuse gliomas into sub-types. We are specifically interested in the isocitrate dehydrogenase (IDH) wild-type. A third of GBM are still non operable, because of a functional critical location which impedes the resection, or because of patient co-morbidity. Non-operable cases allow longitudinal data of glioblastoma evolution, on a patient specific basis. Hence, they are of critical interest for modeling and forecasting processes.

GBM have received a large attention of the modeling community. In 2021, a efficient review of glioblastoma modeling was made by Falco *et al.* in [4]. New hypotheses may emerge from *in silico* studies and treatment personalization may be facilitate by the exploration *in silico* of the parameters' space of the patient. This highly lethal disease and the absence of improvement of its survival rate made these two challenges particularly urgent. The model presented in this article belongs to the category of continuous model, that is to say, the cancerous disease is considered at the tissue scale and modeled as a physical system. As the model is initialized and calibrated by the means of clinical imaging data, it

also belongs to the category of image-informed models. This modeling framework was first developed in 2002, and applied to low and high grade gliomas, by Swanson *et al.* in [5], and after in [6–8]. Since 2013, with the progress of imaging methods, this framework has been developed by Yankeelov *et al.* (see [9]), and applied with clinically-relevant results in various locations such as breast cancer [10] or prostate cancer [11]. Image-informed glioblastoma modeling have been extensively used in the last decades, and have led to personalized modeling in tumor forecasting and treatment response [12–14], and to the inclusion of tissue anisotropy [15], among others hypotheses. In 2020, a specific review of image-informed glioblastoma modeling was made by Mang *et al.* in [16].

We propose in this article a novel image-informed glioblastoma model subjected to a reactive multiphase poromechanical framework. Poromechanics offers to model in a monolithic manner both tissue deformation and pressure-driven fluid flows, these phenomena existing simultaneously in cancer disease. Poromechanics is already applied in cancer modeling, *in vitro* [17, 18] and in animal model [19]. However, except a proposition of patient-specific image-informed modeling in [20] with only qualitative results, to our knowledge, there is no example of this framework applied to glioblastoma modeling in a clinically-relevant and patient-specific basis. Additionally to the description of the brain tissue as a porous medium, our model relies on two biological hypotheses responsible of the heterogeneity of the GBM: hypoxia consequences [21] and extra-cellular matrix (ECM) mechano-biology [22].
The simulation are calibrated against clinical imaging three months after the initial time. Through patient's segmentations, the quantities evaluated are the overlapping of the tumors, clinical and numerical, and of the necrotic cores. A subset of the parameters of the model is initialized and calibrated with the patient imaging data at the initial time. Beforehand, another subset was fixed by a previous work [23]. It is the reproduction of *ex vivo* cortex tissue mechanical testing of Franceschini *et al.* [24] and Budday *et al.* [25]. These parameters represent general mechanical properties and defined the poromechanical core of the model. Even if one may point out the limitation of *ex vivo* results in *in vivo* simulations, these parameters were previously fixed by theoretical studies of poromechanics [17, 26, 27]. Now their values correspond, at least, to *ex vivo* experimental data on human cortex tissue.

First, we briefly present the GBM IDH wild-type and its management, followed by the presentation of the mathematical model, the patient dataset, and the calibration process of the simulation. The results section gives the solution sensitivity on parameters variation and error of the model measured against clinical evidence. Mathematical verification, such as solution sensitivity on mesh refinement, and boundary condition influence are provided. As this work is only a first step of the inclusion of poromechanics in image-informed glioblastoma modeling, we discuss the improvements and further propositions for this inspiring modeling framework.

1 Description of the GBM IDH wild type

Glioma may originate from three sources [28]:

- neural stem cells, embryonic cells located in ventricular and subventricular zones of the brain, which give rise to both neurons and glial cells.

- oligodendrocyte precursor cells, a subset of glial cells precursor specific to oligodendrocytes.

- astrocyte, for which a specific precursor is not yet identified.

Determined the cellular population, and mutations is this population, that give rise to glioma remains the open debate [28]. However, already developed GBM have an astrocytic profile. This profile is characterized by a high heterogeneity both genetic and phenotypic, which creates difficulties both on origin determination and therapeutic design. Among diffuse glioma, GBM is by far the most common (90%). Its incidence represents the majority all kind of glioma and almost the majority of all primary malignant brain tumor. The median age at diagnosis is 65 years and the male incidence is 50% higher than female. Except radiation and rare genetic syndromes, there is not validated risk factor. Since 2005, its standard of care is, if possible, surgical resection followed by a six 1-week cycles of concomitant radiotherapy and temozolomide chemotherapy [29], denoted RT-TMZ treatment. The TMZ is used as a radio sensitizer, and after the 6 cycles, TMZ is used as maintenance from six to twelve months. Despite improvement of

the median survival, now > 15 months, glioblastoma still have a poor prognosis, with a 5-year survival rate at 5.8%, constant since 2000 [2].

The 2016 WHO classification includes now molecular biomarkers, which define GBM subtypes. The first subtype is defined by the status of isocytrate dehydrogenase (IDH). Non-mutated, the subtype is termed wild-type, other subtypes are mutated IDH-1 or IDH-2. IDH 1, 2 or 3 are enzymes involved in cell metabolism. Mutation of IDH 1 or 2 lead to the accumulation of an inhibitor of glioma stem cell differentiation, but also can promote tumor microenvironment. However, IDH mutants represent 10% of glioblastoma and have a better prognosis, as they are less resistant to chemotherapy and provoke better immune response [30]. It shoud be noted that the inevitable recurrence of the GBM will ultimately lead to a dominant wild-type *i.e.*, non-mutated IDH. For the sake of brevity, GBM IDH wild-type will be thereafter abbreviate GBMwt. The second subtype is defined by the status of the O^6-methylguanine–DNA methyltransferase (MGMT), mythelated or non-methylated. The MGMT gene encodes a DNA-repair protein, therefore a high MGMT activity in cancer creates a resistant phenotype both on chemo- and radiotherapy. MGMT activity can be silenced by methylation and it decreases the DNA-repair activity [31]. The methylation of MGMT, termed m-MGMT, represents around 25% of GBM cases. This marker will influence the patient response to the RT-TMZ treatment, as a m-MGMT profile will be more sensitive to RT effect [32]. The IDH mutations and the MGMT methylation status are not correlated, both types of markers can co-exist.

The staging of GBM is first based on the presence of a necrotic core and/or an abnormal microvasculature. These characteristics indicate that hypoxia management is a key feature of GBM. Barnes *et al.* show in [22] that hypoxia applied on GBMwt cells provokes structural changes on the surrounding ECM. The brain ECM has a specific composition. Conversely to the usual rich fibrillar component such as collagen in ECM, brain ECM is almost entirely composed of glycosaminoglycans, a non-fibrous component which plays the mechanical role of shock-absorber. GBMwt cells subjected to a hypoxic environment modify the structure of glycosaminoglycans. Hypoxia signaling is made through hypoxia-inducible factor-1α (HIF1α), which provokes the production by the GBMwt cells of the glycoprotein tenascin-C. The tenascin-C modifies the surronding glycosaminoglycans, leading to a cross-linked, stiffer ECM. This ECM stiffening will ultimately lead to an environment with a higher mechanical stress. Conversely, GBM cells with IDH mutated status have a reduced capacity to produce both HIF1α and tenascin-C. Therefore, this high stiffness of the tumorous tissue is characteristic of GBMwt.

2 Reactive poromechanical modeling of GBM IDH wild-type

The model presented in this section belongs to the category termed as image-informed reactive multiphase poromechanics. Let describe each part of this category:

- poromechanics: the physical system is considered as a composite continuum composed of a permeable and deformable solid scaffold in which and through which fluid flows.

- multiphase: solid and fluid compartments are composite. The solid fraction, which could be compared to the medical definition of the stroma, is made of different and distinct materials (epithelial tissue, ECM - itself composite -, wall vessels, to name a few). Likewise, the fluid fraction is composed of different phases (interstitial fluid, immune cells, tumor cells). It should be noted that the blood is not modeled as a circulating fluid in this model.

- reactive: the modeling of living tissue implies the biological interactions of many diffusive chemical agents (oxygen, cytokines), which can belong to any phase of the system. Their own dynamics are strongly coupled with the poromechanical system. The model also includes non-diffusive reaction as mechanically-induced phenotype switch and hypoxic-induced necrosis.

- image-informed: in order to simulate patient-specific cases, the initial conditions and the boundary conditions of the problem are provided by the patient MRI measurements. A subset of the model's parameters is fixed by these measurements, another subset is calibrated with them.

After the detailed description of the mathematical model, the patient MRI dataset is presented. To conclude this section, the initial settings of the model's parameters, their source and justification, are provided.

General framework

Phases

s	solid
l	lymphatic/interstitial fluid
h	healthy
t	tumor

Volume fraction

ε^s	solid scaffold: stroma and vascular network
ε	extra vascular porosity

Phase Fraction

ω^b	vascular fraction of solid scaffold
ω^{nl}	nutrient fraction of interstitial fluid
ω^ρ	fraction of GBM cells expressing IDH wild type phenotype
ω^N	fraction of necrotic GBM cells

Mass terms and coefficients

$\overset{i \to j}{M}$	mass exchange from phase i to phase j
$\overset{i \to j}{\gamma}$	mass exchange rate from phase i to phase j
$\overset{i \to j}{\zeta}$	dimensionless coefficient from phase i to phase j
r^i	intra-phase mass exchange of phase i
ζ^i	intra-phase dimensionless coefficient of phase i

Font

Italic	scalar quantity s
Bold	vectorial quantity $\mathbf{v}$
$n > 1$ overlines	n^{th} order tensorial quantity: 2nd order $\bar{\bar{T}}$
One overline	homogenized quantity

Let ε^s, the volume fraction occupied by the solid scaffold and ε, the volume fraction occupied by the fluid phases.

$$\varepsilon + \varepsilon^s = 1 \tag{1}$$

The vascular network ω^b is considered as a fraction of the solid scaffold, its volume fraction is denoted $\omega^b \varepsilon^s$.

Considering the fluid phases (t, tumor, h, healthy and l, fluid) and defining their own saturation degree as $S^\beta = \varepsilon^\beta / \varepsilon$ (with $\beta = t, h, l$ the index associated to extra-vascular fluids), we obtain:

$$S^l + S^t + S^h = 1 \tag{2}$$

The thermodynamically constrained averaging theory (TCAT) [33] framework defines the spatial form of the mass balance equation for an arbitrary phase α

$$\underbrace{\frac{\partial \left(\varepsilon^\alpha \rho^\alpha \right)}{\partial t}}_{\text{Accumulation rate}} + \underbrace{\nabla \cdot \left(\varepsilon^\alpha \rho^\alpha \mathbf{v}^{\overline{\alpha}} \right)}_{\text{Outward of phase flow}} - \underbrace{\sum_{\kappa \in \Im_{c\alpha}} \overset{\kappa \to \alpha}{M}}_{\text{Interphase mass transport}} = 0 \tag{3}$$

Representative Elementary Volume
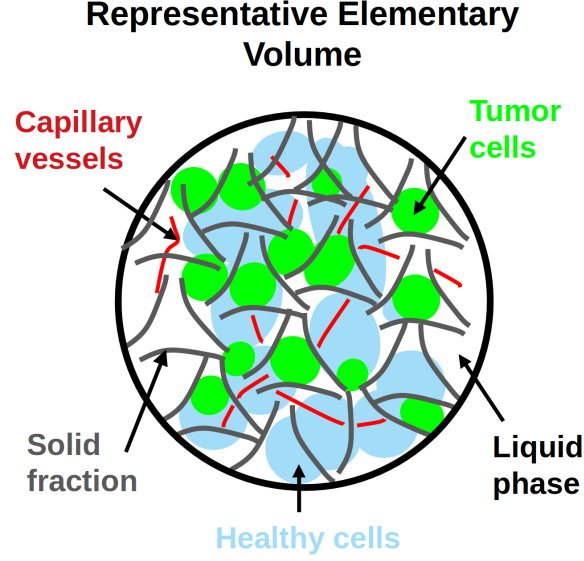
Figure 1:

where ρ^α is the density, $\mathbf{v}^{\overline{\alpha}}$ is the local velocity vector, $\overset{\kappa\to\alpha}{M}$ are the mass exchange terms accounting for transport of mass at the $\kappa\alpha$ interface from phase κ to phase α, and $\sum\limits_{\kappa\in\mathfrak{S}_{c\alpha}}$ is the summation over all the phases sharing interfaces with the phase α.

An arbitrary species i dispersed within the phase α has to satisfy mass conservation too. The following spatial equation is derived following TCAT

$$\underbrace{\frac{\partial\left(\varepsilon^\alpha\rho^\alpha\omega^{\overline{i\alpha}}\right)}{\partial t}}_{\text{Accumulation rate}} + \underbrace{\nabla\cdot\left(\varepsilon^\alpha\rho^\alpha\omega^{\overline{i\alpha}}\mathbf{v}^{\overline{\alpha}}\right)}_{\substack{\text{Outward of species}\\\text{advective transport}}} + \underbrace{\nabla\cdot\left(\varepsilon^\alpha\rho^\alpha\omega^{\overline{i\alpha}}\mathbf{u}^{\overline{\overline{i\alpha}}}\right)}_{\substack{\text{Outward of species}\\\text{diffusive transport}}} - \underbrace{\varepsilon^\alpha r^{i\alpha}}_{\substack{\text{Intraphase reactive}\\\text{exchange of mass}}} + \underbrace{\sum\limits_{\kappa\in\mathfrak{S}_{c\alpha}}\overset{i\alpha\to i\kappa}{M}}_{\substack{\text{Interphase mass transport}\\\text{of the species}}} = 0$$

$$(4)$$

where $\omega^{\overline{i\alpha}}$ identifies the mass fraction of the species i dispersed with the phase α, $\varepsilon^\alpha r^{i\alpha}$ is a reaction term that allows to take into account the reactions between the species i and the other chemical species dispersed in the phase α, and $\mathbf{u}^{\overline{\overline{i\alpha}}}$ is the diffusive velocity of the species i. $\overset{i\alpha\to i\kappa}{M}$ are mass exchange terms accounting for mass transport of species i at the $\kappa\alpha$ interface from phase α to phase κ.

Governing equations

The solid scaffold being deformable, we use the chain rule to define the material derivative:

$$\frac{D^\alpha f^\pi}{Dt} = \frac{\partial f^\pi}{\partial t} + \nabla f^\pi\cdot\mathbf{v}^\alpha \tag{5}$$

And apply it on eqn. 3 and 4

We define the mass conservation of phases by using eq. 5 to express derivatives with respect of the solid phase ε^s. Introducing extra-vascular porosity ε and the saturation degrees of its phases t, h, and l, the mass balance equations of s, t, h and l phases read:

$$\frac{D^s}{Dt}\left(\rho^s\varepsilon^s\right) + \rho^s\varepsilon^s\nabla\cdot\mathbf{v}^{\overline{s}} = \overset{t\to s}{M} \tag{6}$$

$$\frac{D^s}{Dt}\left(\rho^t\varepsilon S^t\right) + \nabla\cdot\left(\rho^t\varepsilon S^t\mathbf{v}^{\overline{ts}}\right) + \rho^t\varepsilon S^t\nabla\cdot\mathbf{v}^{\overline{s}} = \overset{l\to t}{M} - \overset{t\to s}{M} \tag{7}$$

5

$$\frac{\mathrm{D}^s}{\mathrm{Dt}}\left(\rho^h \varepsilon S^h\right) + \nabla \cdot \left(\rho^h \varepsilon S^h \mathbf{v}^{\overline{hs}}\right) + \rho^h \varepsilon S^h \nabla \cdot \mathbf{v}^{\overline{s}} = 0 \tag{8}$$

$$\frac{\mathrm{D}^s}{\mathrm{Dt}}\left(\rho^l \varepsilon S^l\right) + \nabla \cdot \left(\rho^l \varepsilon S^l \mathbf{v}^{\overline{ls}}\right) + \rho^l \varepsilon S^l \nabla \cdot \mathbf{v}^{\overline{s}} = -\overset{l \to t}{M} \tag{9}$$

This system can be resume as follow:

- tumorous phase takes its mass from interstitial fluid phase $\overset{l \to t}{M}$

- tumorous phase produce solid (fibrous) components $\overset{t \to s}{M}$

- healthy cellular phase is considered at the equilibrium

The porous system is modelled as a continuum, under the linear momentum conservation:

$$\mathrm{Div}\, \mathbf{t}^{\bar{T}} = 0 \tag{10}$$

We assume here that all phases are incompressible. However, the overall multiphase system is not incompressible, because of the presence of porosity that evolves according to the scaffold deformation. As all phases are incompressible, their densities ρ^α (with $\alpha = s, t, l$) are constant and the Biot's coefficient $\beta = 1$. With these premises, the total Cauchy stress tensor appearing in eqn 10 is related to the Biot's effective stress as follows

$$\mathbf{t}^{\bar{E}} = \mathbf{t}^{\bar{T}} + \beta p^s \bar{\bar{\mathbf{1}}}, \tag{11}$$

where $p^s = S^l p^l + S^t p^h + S^t p^h$ is denoted the solid pressure, describing the interaction between the fluids and the solid scaffold.

Mass conservation equations of species
The only diffusive specie considered, Oxygen, mass fraction denoted $\omega^{\overline{nl}}$, is governed by advection-diffusion of phase l, the interstitial fluid. The specie is produced by micro-capillaries of the solid fraction phase ω^b, and absorbed by t and h, tumor and healthy cells, its mass balance reads

$$\rho \varepsilon^l \frac{\partial^s \omega^{\overline{nl}}}{\partial \mathrm{t}} + \nabla \cdot \left(\rho \varepsilon^l \omega^{\overline{nl}} \mathbf{u}^{\overline{nl}}\right) + \varepsilon^l \rho \mathbf{v}^{\overline{ls}} \cdot \nabla \omega^{\overline{nl}} = \overset{b \to nl}{M} - \overset{nl \to t}{M} - \overset{nl \to h}{M} + \omega^{\overline{nl}}\overset{l \to t}{M} \tag{12}$$

Internal variables

Hour-based updates Two internal variables, the necrotic fraction $\omega^{\bar{N}t}$ and the Young's Modulus of the ECM E^{ECM}, are updated every 250 minutes, *i.e.* every 10 iterations. This corresponds to physical quantities that have a slower than the primary unknowns (the displacement field, the pressures of the fluids and the level of oxygen). In the following equations, $T = 250\,\mathrm{min}$. For the internal variable $\omega^{\bar{N}t}$, we obtain:

$$\frac{D^s}{DT}\left(\rho^t \omega^{\bar{N}t} \varepsilon S^t\right) + \nabla \cdot (\rho^t \omega^{\bar{N}t} \varepsilon S^t \mathbf{v}^{\bar{t}s}) + \rho^t \omega^{\bar{N}t} \varepsilon S^t \nabla \cdot \mathbf{v}^{\bar{s}} = \varepsilon^t r^{Nt}, \tag{13}$$

with the necrotic growth rate r^{Nt} to calibrated.

The stiffening of the ECM reads is modelled as follows:

$$E_{t+T}^{ECM} = E_t^{ECM} + (1 - \frac{E_t^{ECM}}{E_{\mathrm{idh}}})\mathcal{H}(E_t, E_{\min}, E_{\mathrm{idh}})\langle \omega_{\mathrm{crit}} - \omega^{\bar{n}l}\rangle^+ \tag{14}$$

with $E_{\min}$ is fixed at the lower bound of the stiffness measured in the cortex tissue $E_{\min} = 1.2\mathrm{kPa}$ and E_{idh}, the stiffness of cross-linked ECM, to calibrated.

6

Daily-based updates Two other internal variables, the fraction of GBMwt cells expressing a malignant phenotype ω^ρ and the administration of the RT-TMZ treatment are updated on a daily basis.

ω^ρ is updated every 4.5 days, which corresponds to 260 iterations. We note a lack of quantitative information about phenotype switch in experimental literature. However, we found that at the cell's scale, phenotype switch can be measure in minutes and hour [34]. The only example we found at the macroscale is about lung cancer cells, where the effects of a phenotype switch is observable after a minimum of 72 hours [35]. In the absence of further information on GBMwt cells, we keep our range $T = 4.5$ days. If tumorous area undergo a high osmotic pressure, *i.e.* greater than the threshold p_{IDH}, and a chronic hypoxia, during the period T, a fraction of IDH wild-type cells ω^ρ changes their phenotype. This fraction is updated as follows:

$$\omega_{t+T}^\rho = \omega_t^\rho + \zeta^\rho (1 - \omega_t^\rho)\langle p^t - p_{\text{IDH}}\rangle^+ \langle \omega_{\text{crit}} - \omega^{\bar{n}l}\rangle^+ \varepsilon S^t \tag{15}$$

with ζ^ρ the phenotype switch rate, εS^t the volume fraction of GBM cells, and $\langle \alpha - \beta \rangle^+ = 0$ if $\alpha < \beta$ and 1 else.

The RT-TMZ treatment is administrated by following the standard of care defined in 2005 in [**?**]: before 1 month after diagnosis, the patient started 6 weekly cycles: 5 daily doses of 2 Gray radiotherapy (RT) concomitant with a daily dose of Temozolomide (TMZ). The second part of the standard treatment, 24 weeks of daily TMZ, is not simulated in this article because there is no patient data at this time point. The patient has an non-methylated MGMT profile, which is more resistant to the RT-TMZ treatment [32]. The treatment is modeled by a long and a short effects. The long effect only affects the tumor growth rate:

$$\tilde{\gamma}_g^t = \gamma_{\text{RT}}\gamma_g^t \tag{16}$$

The short effect provokes the necrosis of the tissues, and preferentially the tumorous ones. In this article, we only model the necrosis of GBMwt cells, with two dependencies. First, the TMZ being transmitted through vascular network, its effect is increase accordingly. Second, the density of tumor cells are known to have a more resistant profile (CITE). These two dependencies are modeled by the following equations:

$$f_{\text{b}} = \zeta^{kill}\omega^b \tag{17}$$

f_{b} represents the vascular dependency of RT-TMZ. ζ^{kill} is the optimal killing rate of cells by RT, ω^b the vascular fraction of the stroma.

$$f_{\text{t}} = \zeta^{kill}\varepsilon S^h \tag{18}$$

f_{t} represents the TC density dependency of RT-TMZ. εS^h is the fraction of healthy cells.
RT-TMZ short effect on the necrotic fraction $\omega^{\bar{N}t}$ is modeled by the following equation, the period $T = 1$ days, 5 days per week:

$$\omega_{t+T}^{\bar{N}t} = \omega_t^{\bar{N}t}(1 - \omega_t^{\bar{N}t})(f_{\text{b}} + \text{N}_{\text{mgmt}}f_{\text{t}}) \tag{19}$$

with N_{mgmt}, the negative status of the methylation of MGMT.

Constitutive relationships

Stress-strain relationship For the solid scaffold deformation, the chosen closure relationship for the effective stress $\mathbf{t}^{\bar{\bar{E}}}$ is linear elastic:

$$\mathbf{t}^{\bar{\bar{E}}} = \lambda tr(\epsilon)\bar{\bar{\mathbf{1}}} + 2\mu\epsilon \tag{20}$$

with $\bar{\bar{\mathbf{1}}}$ the identity tensor, $\epsilon(\mathbf{u^s}) = \frac{1}{2}(\nabla \mathbf{u}^s + (\nabla \mathbf{u}^s)^T)$ the linearised strain tensor, and the Lamé constant $\lambda = \dfrac{E\nu}{(1+\nu)(1-2\nu)}$ and $\mu = \dfrac{E}{2(1+\nu)}$.

Generalized Darcy's law The three fluid phases have their own relative permeabilities:

$$k_{\text{rel}}^l = (S^l)^{A_l} \qquad k_{\text{rel}}^h = (S^h)^{B_g} \qquad k_{\text{rel}}^t = (S^t)^{B_g} \tag{21}$$

with A_l and B_g - common to the glial and glioma - to be calibrated.

The interaction between fluid phases and the solid scaffold are modeled by a generalized Darcy's flow, deduced from the linear momentum conservation of fluid phases. The details of this constitutive relationship are provided in [36] and [18].

$$-\frac{k_{\text{rel}}^\alpha k_{\text{int}}^s}{\mu^\alpha} \nabla p^\alpha = \varepsilon S^\alpha (\mathbf{v}^{\bar{\alpha}s}) \qquad \alpha = g, l \tag{22}$$

where k_{int}^s is the intrinsic permeability of the solid scaffold, μ^α, k_{rel}^α and p^α are respectively the dynamic viscosity, relative permeability and the pressure of each fluid phase $\alpha = l, h, t$.

Pressures-saturations relationships The porosity is saturated by three immiscible fluid phases, and each phase having its own pressure, three capillary pressures p^{ij}, *i.e.* pressure difference between fluid i and fluid j, can be defined

$$p^{hl} = p^h - p^l \qquad p^{th} = p^t - p^h \qquad p^{tl} = p^t - p^l \tag{23}$$

As in [37], we assume here that IF is the wetting fluid, HC is the intermediate-wetting fluid and TC the non-wetting one. Only two between the previously defined capillary pressures are independent since

$$p^{tl} = p^{hl} + p^{th} \tag{24}$$

The two capillary pressure-saturation relationships read

$$S^l = 1 - \left[\frac{2}{\pi} \arctan\left(\frac{p^{hl}}{a}\right)\right] \tag{25}$$

$$S^t = \frac{2}{\pi} \arctan\left(\Gamma \frac{p^{th}}{a}\right) \tag{26}$$

where a is a constant parameters depending on ECM microstructure, and Γ is the ratio of HC-IF and TC-HC interfacial tensions (GIUSEPPE do you have info on biological consideration of Γ value? 6 for invasive species).

Malignant cells mobility The fraction of GBMwt cells that expressed a malignant phenotype, ω^ρ, influences the dynamic viscosity of the GBM phase, these cells being more mobile. Beforehand, the dynamic viscosity of the GBM phase is the same than healthy glial cells μ_h, the influence of the malignant cells fraction follows this equation:

$$\mu_t = \mu_h (1 - \omega_\mu^\rho \omega^\rho) \tag{27}$$

where ω_μ^ρ is the coefficient of this influence to calibrated.

Nutrient diffusion The tumor cells growth, metabolism and necrosis are regulated by a variety of nutrient species and intracellular signalling. Two pathways are proposed in the models: one considered nutrient, the oxygen, regulating growth, hypoxia and neo-angiogenesis, and IDH phenotype switch, regulating apoptosis inhibition and cell mobility. For the oxygen diffusion, the Fick's law adapted to a porous medium, was adopted to model diffusive flow of oxygen eq.12:

$$\omega^{\bar{n}l} \mathbf{u}^{\bar{n}l} = -D^{nl} \nabla \omega^{\bar{n}l} \tag{28}$$

where D^{nl} the diffusion coefficient for oxygen in the interstitial fluid is defined by the constitutive equation from [37]

$$D^{nl} = D_0^{nl} (\varepsilon S^l)^\delta, \tag{29}$$

where $D_0^{nl} = 2.5 \cdot 10^{-9}$ corresponding to the the ideal case of oxygen diffusion in pure water, *i.e.* with $\varepsilon S^l = 1$, at $37°$ [38]. The exponent δ is equal to 2, to account for the tortuosity of cell-cell interstitium where oxygen diffuse [17].

Tumor cells growth and metabolism Tumor cell growth is related, for its main part, to the exchange allowed by oxygen between the IF and the living fraction of the tumor. For its smaller part, it is related to the exchange allowed by other nutrients (*e.g.*, glucose) in hypoxic situation, between the IF and the positive phenotype IDH fraction of the living tumor. The total mass exchange from IF to the tumor cell phase is defined as

$$\sum_{i \in l} \overset{i \to t}{M} = \overset{i \to t}{\underset{\text{Oxy}}{M}} + \overset{i \to t}{\underset{\text{Fat}}{M}} \tag{30}$$

$$\overset{i \to t}{\underset{\text{Oxy}}{M}} = \overset{l \to t}{\gamma} \varepsilon S^t (1 - \omega^N) \mathcal{H}_p(p^t) \mathcal{H}(\omega^{\bar{n}l}) \tag{31}$$

$$\overset{i \to t}{\underset{\text{Fat}}{M}} = \overset{l \to t}{\gamma} \varepsilon S^t (1 - \omega^N) \omega_{\text{A}}^\rho \omega^\rho \mathcal{H}_p(p^t) \tag{32}$$

where $\overset{i \to t}{\underset{\text{Oxy}}{M}}$ represents the nutrient pathway of TC metabolism and $\overset{i \to t}{\underset{\text{Fat}}{M}}$ the anoxic growth part due to lipids synthesis of TC positive IDH phenotype [39].

$\overset{l \to t}{\gamma}$ is the tumor growth rate parameter, $\varepsilon S^t (1 - \omega^N)$ is living fraction of the tumor, ω^ρ, its positive IDH phenotype fraction and ω_{A}^ρ, their apoptosis inhibited fraction.

$\mathcal{H}$ and $\mathcal{H}_p$ are regularized step functions varying between 0 and 1, with two threshold parameters σ_1, σ_2, *i.e.* $\mathcal{H} = \mathcal{H}(\sigma, \sigma_1, \sigma_2)$. When the variable σ is greater than σ_2, $\mathcal{H}$ is equal to 1, it decreases progressively when the variable is between σ_1 and σ_2 and is equal to zero when the variable is lower than σ_1. $\mathcal{H}$ represents the growth dependency to oxygen:

$$\mathcal{H}(\omega^{\bar{n}l}, \omega_{\text{crit}}, \omega_{\text{env}}) = \begin{cases} 0 & \text{if} \quad \omega^{\bar{n}l} \leq \omega_{\text{crit}} \\ \\ \dfrac{1}{2} - \dfrac{1}{2} \cos\left(\pi \dfrac{\omega^{\bar{n}l} - \omega_{\text{crit}}}{\omega_{\text{env}} - \omega_{\text{crit}}}\right) & \text{if} \quad \omega_{\text{crit}} \leq \omega^{\bar{n}l} \leq \omega_{\text{env}} \\ \\ 1 & \text{if} \quad \omega^{\bar{n}l} \geq \omega_{\text{env}} \end{cases} \tag{33}$$

ω_{env}, the optimal oxygen mass fraction, is set to $4.2 * 10^{-6}$ which corresponds, according to Henry's law, to 90mmHg, the usual oxygen mass fraction in arteries (see [40]). ω_{crit}, the hypoxia threshold, is cell-line dependent, for tumor cells, it has been set to a very low value: 10^{-6} ($\approx$ 20mmHg, for common human tissue cells, hypoxic level is defined between 10 and 20mmHg [41]) Function $\mathcal{H}_p$ represents the dependency on pressure:

$$\mathcal{H}_p(p^\alpha, p_{\text{IDH}}, p_{\text{crit}}) = \begin{cases} 1 & \text{if} \quad p^\alpha \leq p_{\text{IDH}} \\ \\ \sqrt{\dfrac{p_{\text{crit}} - p^\alpha}{p_{\text{crit}} - p_{\text{IDH}}}} & \text{if} \quad p_{\text{IDH}} \leq p^\alpha \leq p_{\text{crit}} \\ \\ 0 & \text{if} \quad p^\alpha \geq p_{\text{crit}} \end{cases} \tag{34}$$

Before phenotype switch, IDH wild-type GBM cells are known to produce an important quantity of stroma [22]. Hence, a part of the mass growth term related to oxygen metabolism $\overset{l \to t}{\underset{\text{Oxy}}{M}}$ is converted into stroma:

$$\overset{t \to s}{M} = \overset{t \to s}{\zeta} \overset{l \to t}{\underset{\text{Oxy}}{M}} \tag{35}$$

As tumor grows, oxygen is taken up from the IF and produce by the vascular fraction of the solid scaffold, so that the sink and source terms in eq.12 take the following form:

$$\overset{nl \to t}{M} = \overset{nl \to t}{\gamma} \varepsilon S^t (1 - \omega^N) \langle \omega^{\bar{n}l} - \omega_{\text{crit}} \rangle^+ \mathcal{H}_p(p^t), \tag{36}$$

9

$$\overset{nl\rightarrow h}{M} = \overset{nl\rightarrow h}{\gamma}\varepsilon S^h \langle \omega^{\bar{n}l} - \omega_{\text{crit}} \rangle^+ \mathcal{H}_p(p^h), \tag{37}$$

$$\overset{b\rightarrow nl}{M} = \overset{b\rightarrow nl}{\gamma}\varepsilon^s \omega^b \langle \omega_{\text{env}} - \omega^{\bar{n}l} \rangle^+ \tag{38}$$

with $\overset{i\rightarrow j}{\gamma}$ the correspond mass exchange rate form phase i to phase j, where the term $\varepsilon S^t(1 - \omega^N)$ is the volume fraction of living tumor cells, εS^h the volume fraction of healthy cells and $\varepsilon^s \omega^b$ the volume fraction of vascularized stroma.

3 Patient specific image-informed modeling

VINCENT: brief presentation of the patient profile

Patient dataset

The dataset is composed of MRI methods with a resolution of $256 \times 256 \times 200$. They are displayed Figure 2. The dataset contains:

- a segmentation, Fig. 2A, by DeepMedic convolutional neural network [42], cleaned by authors of this article. The segmentation gives edema, tumor and necrosis. The segmentation is performed by using the T1 Gadolinium contrast enhanced (T1-CE) method, Fig. 2C, and the very long sequence T2 fluid attenuated inversion recovery (FlAIR) method, Fig. 2D.

- a registration, Fig. 2B, by FAST hidden Markov chain [43], which only inform about grey and white matter, as the tumor tissue is partially misinterpreted as CSF. FAST uses T1-CE method for its registration.

- a diffusion weighted MRI method, termed as apparent diffusion coefficient (ADC) of water, Fig. 2E.

- a perfusion MRI method, termed as relative cerebral blood volume (rCBV), Fig. 2F.

This dataset is given at two time points: pre-operative examination and after the 6 cycles of RT-TMZ therapy. 63 days separates the two time points. The first point is used for initial conditions of the model, the second point for the calibration of the parameters.

The region of interest (ROI) shown Figure 3A, defined in accordance with the surgical practice CITE, corresponds to the segmented volume of the constrast-enhanced tumor plus 2 cm margin around this volume, where a GBM has the greater probability to progress. Nevertheless, this margin by no means presumes of the size of the computational domain, Figure 3B. Indeed, the influence of the prescribed boundary conditions on the GBM evolution is measured separately (see Appendix A).

Initial parameters setings

The quantities and methods are summarized Table 3 and 2.

Segmentation Tumor segmentation with Deep Medic and brain registration with FAST give two distinct partitions of the computational domain Ω:

- Deep Medic partition gives Ω_{CE}, the GBM Contrast Enhanced non-necrotic domain, Ω_N, the GBM necrotic domain, Ω_E the GBM edema domain and Ω_O the outer segmentation domain. The Deep Medic partition is defined by $\Omega_{CE} \cup \Omega_N \cup \Omega_E \cup \Omega_O = \Omega$

- FAST partition gives Ω_{CSF}, the CSF compartment of the patient brain -which cannot be exploited due to tumor tissue-, Ω_G, the grey matter subdomain and Ω_W the white matter subdomain. The FAST partition is defined by $\Omega_{CSF} \cup \Omega_G \cup \Omega_W = \Omega$
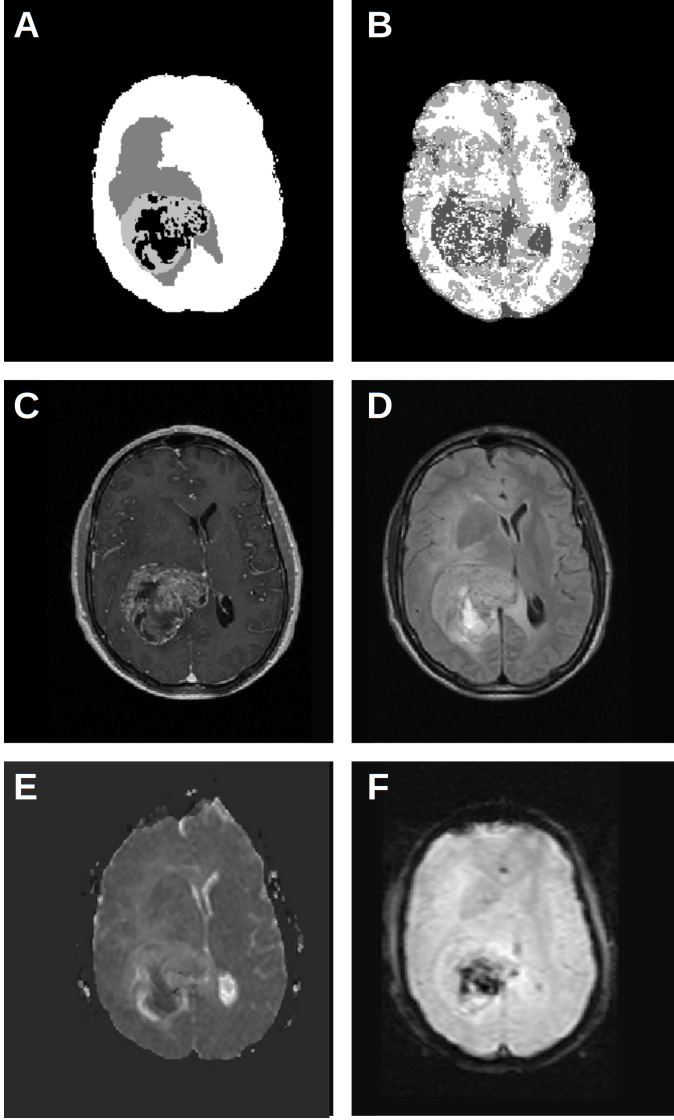
Figure 2: **Patient imaging dataset.** **A** DeepMedic segmentation gives brain mask (white), edema (dark grey), tumor (light grey) and necrotic (black) zones. **B** FAST segmentation gives only grey and white matter zones, as the tumor tissue is partially misinterpreted as CSF (dark grey). **C** T1-CE method gives the density of solid components (brighter contrast, higher density). **D** FlAIR method gives the density of fluid components (brighter contrast, higher density). **E** ADC method gives diffusion coefficient of water (brighter contrast, higher coefficient). **F** r-CVB method gives the permeability between intra- and extra-vascular space (brighter contrast, higher permeability).

ADC method gives diffusion coefficient of water and it is inversely correlated to cellularity [9]. For this reason, we choose to consider the interstitial fluid (IF) saturation proportional to ADC contrast. As there is the presence of an edema, the maximum contrast $\mathrm{ADC_{max}}$ corresponds to a pathological value of IF pressure. We have set it to $p_{\max} = 400\mathrm{Pa}$ and the minimal value $\mathrm{ADC_{min}}$, which correspond to the maximum cellularity (*e.g.*, the tumor necrotic zones), at a value below normal pressure $p_{\min} = 40\mathrm{Pa}$. Then, we obtain the linear function to prescribe the initial conditions for IF pressure:

$$p_0^l(x,y,z) = \frac{p_{\max}^l - p_{\min}^l}{\mathrm{ADC_{max}} - \mathrm{ADC_{min}}} \left(\mathrm{ADC}(x,y,z) - \mathrm{ADC_{min}}\right) + p_{\min}^l \tag{39}$$

The tumor quantities are defined over $\Omega_{CE} \cup \Omega_N$ so they need both segmentation and MRI methods to be prescribed. In [44], histological cuts on 7 patients with GBMwt gives a volume fraction of GBMwt cells of 0.12 ± 0.07. With the porosity estimation in [23], $\varepsilon = 0.55 \pm 0.05$, it gives the following range of tumor cells saturation S^t $0.24; 0.115$ As base values, we chose the maximum saturation in the necrotic core $S_N^t = 0.24 \in \Omega_N$ and a value slightly below average in the contrast-enhanced zone $S_{CE}^t = 0.165 \in \Omega_{CE}$. The relationship between S^t and TC pressure difference p^{th} depends on two parameters a and Γ. With $a = 550$ and $\Gamma = 6$, we obtain $p_N^{th} = 34\mathrm{Pa}$ and $p_{CE}^{th} = 22\mathrm{Pa}$. These base values are tuned by the mean of
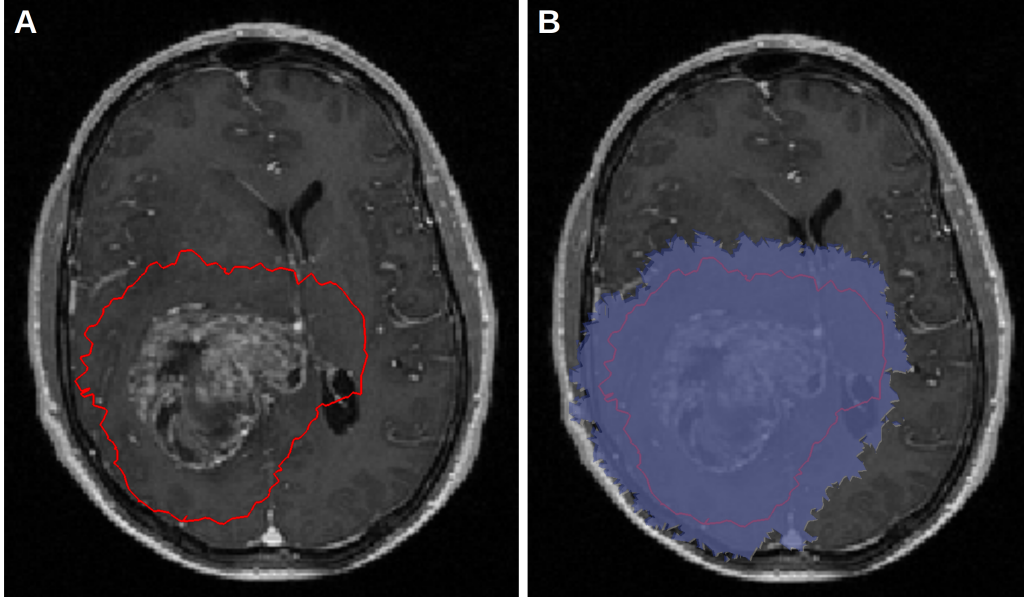
11

Figure 3: **Definition of the region of interest (ROI). A** ROI defined by the clinical margin ($\approx 2\,\mathrm{cm}$ around the tumor zone). **B** Computational domain defined by boundary conditions ($2.27\pm0.3\,\mathrm{cm}$ around the tumor zone) with a negligible sensitivity on the tumor evolution, for further details see appendix A.

the ADC mapping:

$$p_0^{th}(x,y,z) = \begin{cases} p_N^{th}\left(1 - \dfrac{p_0^l(x,y,z)}{p_{\max}^l}\right) & \text{in } \Omega_N \\[3mm] p_{CE}^{th}\left(1 - \dfrac{p_0^l(x,y,z)}{p_{\max}^l}\right) & \text{in } \Omega_{CE} \end{cases} \tag{40}$$

As the saturation of healthy glial cells S^h is constrained by Eq.2, this saturation is not directly linked by the capillary pressure p^{hl} of glial cells. Nevertheless, the interstitial fluid saturation S^l is subjected to p^{hl} Eq.29. The initial mapping of p^{hl} with DeepMedic segmentation and ADC method respects the range of physical values deduced from [23]. In edema zone Ω_E, the base value of p_E^{hl} is fixed at $800\,\mathrm{Pa}$, which gives a pathological value of $S^l = 0.39$. In the rest of the domain $\Omega \setminus \Omega_E$, the base value p_R^{hl} is fixed at $1.6\,\mathrm{kPa}$, which gives a physiological value of $S^l = 0.11$.

$$p_0^{hl}(x,y,z) = \begin{cases} p_E^{hl}\left(1 - \dfrac{p_0^l(x,y,z)}{p_{\max}^l}\right) & \text{in } \Omega_E \\[3mm] p_R^{hl}\left(1 - \dfrac{p_0^l(x,y,z)}{p_{\max}^l}\right) & \text{in } \Omega \setminus \Omega_E \end{cases} \tag{41}$$

The initial value of p^{hl} is also fixed to sustain the intracranial pressure p^s Eq.11 all over the domain. With the initial mapping of p^{hl}, we obtain an average intracranial pressure p^s of $7.75\mathrm{mmHg}$, and of $12.5\mathrm{mmHg}$ in the inner core of the tumor. These values are in balance with clinical measurements (CITE). On fait un point sur CSF ?

The mapping of the intrinsic permeability of the stroma k_{int}^s is performed through FAST registration, as the white matter tracks has a higher permeability [45], and through the ADC method, because we interpret the zones of accumulation of fluids as zones with a higher permeability. As the patient data does not contain a diffusion tensor imaging method, k_{int}^s remains a scalar and heterogeneous quantity, but not a vectorial one. The determination of intrinsic permeability of the brain is a very difficult experimental task, and the wide range of values obtained remains an open debate (see [23] for details). For $k_{\min}^s$, we choose a one order lower value than we found in [23], $k_{\min}^s = 10^{-14}\,\mathrm{m}^2$. For $k_{\max}^s$, we choose the lower

bound of [18], $k^s_{\max} = 10^{-13} \, \mathrm{m}^2$, as the grey and white matter were not distinguished. Where the voxels are labelled as white matter, we follow the trends the results of Jamal *et al.* [45] by prescribing a 15 fold higher value, *i.e.* the maximum value of k^s_{int} is $1.5 \cdot 10^{-12} \, \mathrm{m}^2$.

$$k^s_{\mathrm{int}\,0}(x,y,z) = \begin{cases} \dfrac{k^s_{\max} - k^s_{\min}}{\mathrm{ADC}_{\max} - \mathrm{ADC}_{\min}} \left(\mathrm{ADC}(x,y,z) - \mathrm{ADC}_{\min}\right) + k^s_{\min} & \text{in } \Omega \setminus \Omega_W \\[2ex] 15\left(\dfrac{k^s_{\max} - k^s_{\min}}{\mathrm{ADC}_{\max} - \mathrm{ADC}_{\min}} \left(\mathrm{ADC}(x,y,z) - \mathrm{ADC}_{\min}\right) + k^s_{\min}\right) & \text{in } \Omega_W \end{cases} \tag{42}$$

rCBV method is treated the same way than ADC method. It gives the initial condition of vascular fraction ω^b of the solid scaffold ε^s. The maximum contrast $\mathrm{rCBV}_{\max}$, which corresponds to a neo-vascular network, sets the vascular fraction to $\omega^b_{\max}$. From early work in angiogenesis, Folkman *et al.* in [46] estimated the vascularized fraction of a subcutaneous tissue undergoing angiogenesis to 1.5%, which is 400 fold higher than healthy tissue. However, cortex tissue is already a highly vascularized tissue, with a volume fraction estimated between 3% and 5% (Yiming *et al.* in [47]). We chose to set $\omega^b_{\max} = 0.075$, 50% higher than maximal healthy value, and $\omega^b_{\min} = 0.003$, 10 fold lower than minimal healthy value for poorly vascularized zones. We obtain for the vascular fraction of the solid scaffold:

$$\omega^b_0(x,y,z) = \frac{\omega^b_{\max} - \omega^b_{\min}}{\mathrm{rCBV}_{\max} - \mathrm{rCBV}_{\min}} \left(\mathrm{rCBV}(x,y,z) - \mathrm{rCBV}_{\min}\right) + \omega^b_{\min} \tag{43}$$

General mechanical parameters of cortex tissue were prescribed by a previous article by Urcun *et al.* in [23]. It consisted in the reproduction of two mechanical tests of healthy cortex human and animal: confined compressions ($N = 6$), *i.e.* consolidation tests [24] and indentation tests with several load rates and diameters (N=?). The local sensitivity of the parameters were measured, a part of the results were calibrated and another part validated on external data. All the details are provided in [23]. Regarding this article, it allows reducing the wide range the mechanical parameters of cortex tissue assumed in the literature (CITE,CITE,CITE), and more specifically in the poromechanical literature (CITE,CITE,CITE). Although individual variation could be considered, these parameters are related the general mechanical behavior of healthy tissue. They are presented Table 1. These background parameters will be thereafter considered as fixed.
Un point sur les parameters
Un point sur les parameters theoriques

Partial resolution of the mathematical system Imaging data or mechanical tests do not give information on the initial state of the oxygen fraction $\omega^{\overline{nl}}$. Physiology literature gives information on the bounds of the tumor growth metabolism Eq.33. The hypoxia threshold ω_{crit} is estimated to an oxygen fraction between $7 \cdot 10^{-7}$ and 10^{-6} (CITE). This value corresponds, according to Henry's law, to (TO DO). The oxygen fraction of healthy brain tissue ω_{env} is estimated to $1.9 \cdot 10^{-6}$ (CITE), which corresponds, according to Henry's law, to (TO DO). Nevertheless, between these two bounds, the fraction of oxygen at each voxel of the domain is not known. To fix this, the mathematical system is partially solved. The oxygen fraction is set to 10^{-6} in $\Omega_{CE} \cup \Omega_N$ and to $1.9 \cdot 10^{-6}$ in the remaining part. With these initial conditions, the system is solved with a very small increment of time ($dt = 1 \, \mathrm{s}$), as this initial state is very unstable. Since the system becomes steady, *i.e.* the variation of the oxygen fraction in one second becomes negligible, the simulation is stopped and the solution of $\omega^{\overline{nl}}$ is conserved as initial condition for this unknown. The computation lasts for 90 seconds of simulated time.

The same situation appears for the displacement field $\mathbf{u^s}$, as the previous deformation of the organ are not recorded. Moreover, one can argue that a original displacement field for an organ has no meaning. As the fluid phases exert a pressure on the stroma, the same process than for $\omega^{\overline{nl}}$ is adopted. Since the mechanical steady state is reach between fluid pressures and stroma displacement, the simulation is stopped and the resulting displacement field $\mathbf{u^s}$ is conserved as initial solution for this vectorial unknown. The computation lasts for 6 minutes of simulated time, the initial $\mathbf{u^s}$ reaches a maximum displacement between $50 \, \mu\mathrm{m}$ and $60 \, \mu\mathrm{m}$.

Clinical literature Kitange *et al.* in [48], showed by *In vitro* experiments and animal models that MGMT activity greatly increase the GBM resistance to TMZ treatment. Their statistical analysis of *in vitro* results showed an increase of almost 60% of the surviving GBM cells fraction. Based on these findings, we set the resistant fraction of non-methylated (n-)MGMT to 0.6 as initial guess.

Symb.	Value	Unit	Meaning	Range in literature
ε	0.55 ± 0.05	[1]	Porosity	0.595 ± 0.165
ν	0.48 ± 0.01	[1]	Poisson's ratio	0.47 ± 0.02
E_{Cortex}	3.23 ± 2.8	kPa	Young's Modulus of Cortex tissue	4.5 ± 3.5
k_{Cortex}	$1.5 \pm 1.4 \cdot 10^{-12}$	m^2	Permeability of Cortex tissue	from 10^{-17} to 10^{-13}
S^l	0.07 ± 0.043	[1]	IF saturation	0.149 ± 0.084
μ_l	$5.5 \pm 2.5 \cdot 10^{-3}$	Pa·s	Dynamic viscosity of IF	$0.85 \pm 0.15 \cdot 10^{-3}$
A^l	1	[1]	Exponent of tortuosity for IF	No expe. data
μ_h	32.5 ± 2.5	Pa·s	Dynamic viscosity of HC	No expe. data
B^h	2 or 1	[1]	Exponent of tortuosity for HC	No expe. data
a	600 ± 200	Pa	Cell-ECM ground interaction	No expe. data

Table 1: **Model's parameters estimation by *ex vivo* mechanical testing [23].** For the sources of the literature values, see [23].

Type	Symb.	Unit	Method(s)	Parameter
Material parameters	$k()$	m^2	ADC, Segment. [43]	Permeability mapping
	D_0^{nl}	m^{2}s^{-1}	ADC	O$_2$ diffusion coefficient
	$E()$	Pa	Segment. [42]	Young's Modulus mapping
Initial conditions	p^l	Pa	ADC	Interstitial fluid pressure
	p^{hl}	Pa	ADC, Segment. [42]	Healthy cells pressure
	p^{th}	Pa	ADC, Segment. [42]	Tumor cells pressure
	ω^b	[1]	rCVB	Vascular fraction

Table 2: **Parameters deduced from MRI methods**

In silico reproduction process

Finite element formulation We implemented the above model with Dolfin, the C++ libraries of the FEniCS framework [49]. We used an incremental formulation, *i.e.* $\bar{X}_{n+1} = \bar{X}_n + \delta\bar{X}$, for the mixed finite element (FE) formulation. We resolve the system by the means of a fixed-stress staggered scheme: the pressures are solved with a fixed stress tensor, the stress tensor is solved with the updated pressures, and the loop is subjected to the norm of the solution increment as convergence criterion (for instance, see [50]). All the codes used in this article can be provided upon request.

Boundary conditions Every unknowns are subjected to a homogeneous Dirichlet conditions on the domain boundary. This is a consequence of the incremental formulation. For each unknown α, we prescribed $\delta X_\alpha = 0$ on $\partial\Omega$, the boundary of the domain. In other words, the initial settings of the unknowns remain unchanged at the boundary of the domain during the simulation. The influence of the boundary distance on the FE solution is studied Appendix A.

Quantities evaluated In a multiphase system, grasp the relevant quantities is not always straightforward, for instance, the saturation of tumor cells S^t could be meaningless without the indication of the porosity ε. If we want to delineate a tumor area, the significance of a high S^t could be diminished by a

Type	Symb.	Value	Unit	Meaning	Source
Poromechanical	E_{IDH}	4000	Pa	Young's Modulus of Cross-linked ECM	
	p_{crit}	1530	Pa	Critical threshold of mechanical inhibition	
	Γ	6	[1]	Interfacial tension ratio between HC-IF and TC-HC	
Oxygen biology	$\overset{l\to t}{\gamma}$	$2.16\cdot 10^{-2}$	kg/(m^3.s)	TC growth rate	
	$\overset{nl\to t}{\gamma}$	3.5	s^{-1}	TC oxygen consumption rate	
	$\overset{nl\to h}{\gamma}$	$2.5\cdot 10^{-1}$	s^{-1}	HC oxygen consumption rate	
	$\overset{b\to nl}{\gamma}$	$1.44\cdot 10^{-2}$	s^{-1}	Capillaries oxygen production rate	
	ω_{crit}	$8\cdot 10^{-7}$	kg/m^3	Hypoxic threshold oxygen mass fraction	
ECM mechano-biology	p_{idh}	770	Pa	Phenotype switch mechanical threshold	
	ω_A^ρ	$1\cdot 10^{-1}$	[1]	TC apoptosis inhibited fraction	
	ω_μ^ρ	$9\cdot 10^{-1}$	[1]	TC dynamic viscosity loss fraction	
	$\overset{t\to s}{\zeta}$	$4\cdot 10^{-1}$	[1]	Stroma production coefficient	
	ζ^ρ	6	[1]	Phenotype switch coefficient	
RT-TMZ treatment	ω_{TMZ}^b	0.1	[1]	Vascular threshold for TMZ effect	
	N_{mgmt}	0.6	[1]	Resistant fraction of GBMwt cells to RT-TMZ treatment	

Table 3: **Model's parameters to be calibrated, initial values, and sources**

small ε. Hence, we adopt the following measure for the interpretation of the results: the volume fraction of tumor cells:

$$\text{Vol}_{TC} = \varepsilon S^t \tag{44}$$

Vol_{TC} can be separate in three relevant quantities, the living tumor cells:

$$\text{Vol}_{LC} = \varepsilon S^t (1 - \omega^{Nt}) \tag{45}$$

The malignant tumor cells:

$$\text{Vol}_{mal} = \varepsilon S^t (1 - \omega^{Nt})\omega^\rho \tag{46}$$

The necrotic tumor cells:

$$\text{Vol}_{nec} = \varepsilon S^t \omega^{Nt} \tag{47}$$

Error measure To measure the quality of the numerical results, we followed the prescription of [51]: the root mean square error (RMSE) relative to a reference, which is specified accordingly. The RMSE of the numerical quantity ξ_{num} relative to an experimental reference ξ_{ex}, evaluated at n points is computed as:

$$RMSE(\xi_{\text{num}}, \xi_{\text{ex}}, n) = \sqrt{\frac{1}{n}\sum_{k=1}^{n}\left(\frac{\xi_{\text{ex}}(k) - \xi_{\text{num}}(k)}{\xi_{\text{ex}}(k)}\right)^2} \tag{48}$$

Sensitivity analysis: cost functions and Sobol indices. We performed a local sensitivity analysis to estimate Sobol sensitivity indices on the patient calibration dataset, to assess the sensitivity of the computational outputs to the input parameters. First, we designed the cost function J_{over}, which quantify the error between the numerical results and the patient calibration dataset, by measuring the spatial overlapping.

$$J_{\text{over}} = \frac{\sum_j |\left(\mathbb{1}_{\text{exp}}(j) - \mathbb{1}_{\text{num}}(\text{Vol}_{TC} j)\right)| \Delta_j}{\sum_i \Delta_i} \quad j \in \Omega \tag{49}$$

with

$$\mathbb{1}_{\text{num}}(\text{Vol}_{TC}) \begin{cases} 0 & \text{if} \quad \text{Vol}_{TC} \leq 0.001 \\ 1 & \text{else} \end{cases} \qquad \mathbb{1}_{\text{exp}}(j) \begin{cases} 0 & \text{if} \quad j \notin \Omega_{CE} \cup \Omega_N \\ 1 & \text{else} \end{cases} \tag{50}$$

where Δ_i is the volume of the ith tetrahedron, where $\mathbb{1}_{\text{exp}}(j)$ is the characteristic function of the patient segmentation at the second time point - the calibration dataset -, and $\mathbb{1}_{\text{num}}(\text{Vol}_{TC})$ the characteristic function of the computational GBM at the same time point.

The 13 parameters at their initial values give J_{over}^0 (see Table 3). Then, the 13 parameters are perturbed one at a time of $\pm 10\%$. The cost variation $V_{\text{over}}^{\alpha \pm 10\%}$ of a parameter α is defined by:

$$V_{\text{over}}^{\alpha \pm 10\%} = \frac{J_{\text{over}}^{\alpha \pm 10\%} - J_{\text{over}}^0}{J_{\text{over}}^0} \tag{51}$$

Then, the points of the variation are linearly interpolated. The influence of the parameter α is deduced from the slope θ_α of the linear fit. The first-order Sobol index S_α is calculated as follows:

$$S_\alpha = \frac{\theta_\alpha^2}{\sum_\alpha \theta_\alpha^2} \tag{52}$$

Calibration To minimize J_{over}, we chose the parameters set α_i that gather 90% of the variance, *i.e.* $\sum_i S_{\alpha_i} \geq 0.9$ for the calibration. This parameters set is then calibrated using a classical Newton-Raphson algorithm.

4 Results

Local sensitivity analysis

The results of the first order sensitivity analysis are shown Figure 4, and the values of the Sobol indices Table 4. Two parameters, $\overset{nl \to t}{\gamma}$ and $\overset{nl \to h}{\gamma}$, have a negligible influence on the solution. The parameter p_{idh}, the pressure threshold that mechanically induced the malignant phenotype switch of GBMwt cells is largely dominant in comparison of the others parameters. Finally, only 8 parameters gather 97.5% of the variance: p_{idh} (0.505), ω_{crit} (0.223), Γ (0.068), p_{crit} (0.058), E_{idh} (0.038), ω_A^ρ (0.028), ζ^ρ (0.028) and $\overset{l \to t}{\gamma}$ (0.027). This subset of parameters is calibrated, and the others are fixed.

Calibration

The 8 parameters were identified with a Newton-Raphson algorithm, only 3 iterations were performed for a duration of 12 days of computation time, with the following overlapping errors: $J_{\text{over}}^0 = 0.581$, $J_{\text{over}}^1 = 0.333$, $J_{\text{over}}^2 = 0.270$ and $J_{\text{over}}^3 = 0.188$. Their values are given Table 5. The 3D results at J_{over}^3 are shown Figure 4. At the third iteration, the volume of the simulated tumor is of $118.2\,\text{cm}^3$, the volume of the patient tumor being of $122.5\,\text{cm}^3$. Then, we obtained a tumor with 3.5% of error in volume and which overlaps 81.2% of the patient tumor.
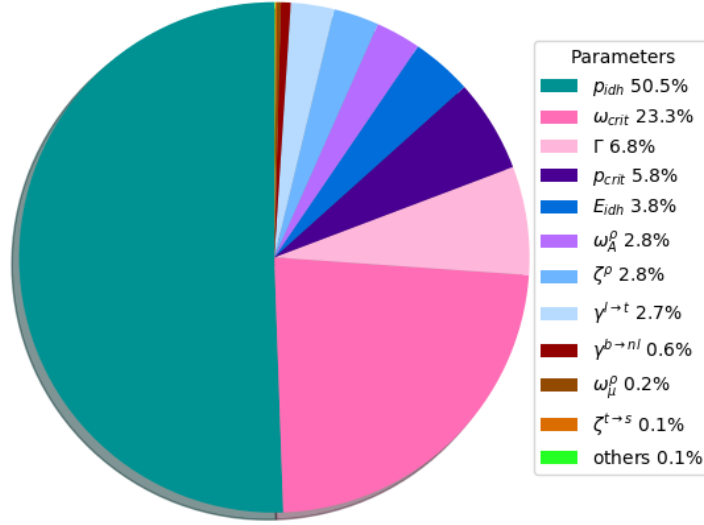
Figure 4: **Sobol indices of the parameters at their initial values.** Details of the parameters Table 4. 8 parameters gather 97.5% of the variance: p_{idh} (0.505), ω_{crit} (0.223), Γ (0.068), p_{crit} (0.058), E_{idh} (0.038), ω_A^ρ (0.028), ζ^ρ (0.028) and $\gamma^{l \to t}$ (0.027). They constitute the parameters subset to calibrate

Qualitative results

Mechanical inhibition of tumor growth   This phenomenon is well documented *in vitro* [52–54] *in vivo* [55], and already used in image-informed model for breast [10] or prostate [11] cancers and were comprehensively reviewed by Jain *et al.* in [56] and more recently by Nia *et al.* [57]. Even if each cell line has its own conditions (inhibiting pressure threshold, share stress dependency, phenotype switch window, coupling phenomena with hypoxia), the mechanical inhibition of tumor growth is now accepted as a shared phenomenon in cancer. Specifically in GBM mechanical growth inhibition, to our knowledge, we report only one quantitative study of Kalli *et al.* [58], which estimates for the GBM A172 cell line an inhibiting threshold $\approx 3.5\,\text{kPa}$. After our calibration of the inhibiting pressure threshold p_{crit}, we see in Figure 4A3 and C3 that several large zones with no progression in the patient data undergo, in the corresponding simulated zones, a pressure at least equal to p_{crit}. However, few zones of progression in the patient data (see Figure 4B3) undergo this inhibiting pressure in the simulation.

Malignant phenotype in tumor growth and treatment response   Several studies [22,59] suggest that this phenotype switch is resulting of an increase of internal stress, denoted tensional homeostasis, coupled with an hypoxic environment. We proposed to model this phenomenon at the macroscale, Figure 4 shows the qualitative results of this part. At $T + 21$ days (Figure 4A1, B1, C1) before RT-TMZ treatment, the malignant GBMwt cells develops at the intersection of high pressure zones (threshold p_{idh}) and hypoxic zones (threshold ω_{crit}). During the 6 cycles of RT-TMZ (Figure 4A2-3, B2-3, C2-3), these zones remain stable, showing that the GBM activity is stopped by the treatment. The resistance of the malignant fraction ω^ρ is given by the fixed parameter N_{mgmt} (see section 3, subsection *Initial parameters setting*). During the 6 cycles of RT-TMZ, the malignant fraction progress in the opposite direction of hypoxic zones, its volume and its density are almost multiply by two.

5   Discussion

In this study we proposed to model a patient-specific non-operable glioblastoma, which subtype is termed as isocitrate dehydrogenase wild-type. The disease was first modeled within a porous medium, pre-

17

Type	Symb.	Value	Sobol indices
Poromechanical	E_{idh}	4000	0.038
	p_{crit}	1530	0.058
	Γ	6	0.068
Oxygen biology	$\overset{l \to t}{\gamma}$	$2.16 \cdot 10^{-2}$	0.027
	$\overset{nl \to t}{\gamma}$	3.5	$< 10^{-4}$
	$\overset{nl \to h}{\gamma}$	$2.5 \cdot 10^{-1}$	$< 10^{-4}$
	$\overset{b \to nl}{\gamma}$	$1.44 \cdot 10^{-2}$	0.006
	ω_{crit}	$8 \cdot 10^{-7}$	0.223
ECM mechano-biology	p_{idh}	770	0.505
	ω_A^ρ	$2 \cdot 10^{-1}$	0.028
	ω_μ^ρ	$9 \cdot 10^{-1}$	0.002
	$\overset{t \to s}{\zeta}$	$4 \cdot 10^{-1}$	0.001
	ζ^ρ	6	0.028

Table 4: **Sobol indices of the parameters at their initial values.** $J_{\mathrm{over}} = 0.581$

Symb.	Value
p_{idh}	970
ω_{crit}	$7 \cdot 10^{-7}$
Γ	5
p_{crit}	1530
E_{idh}	4000
ω_A^ρ	$1 \cdot 10^{-1}$
ζ_A^ρ	2.5
$\overset{l \to t}{\gamma}$	$2.8 \cdot 10^{-2}$

Table 5: **Parameters calibration, $J_{\mathbf{over}} = 0.188$.**

calibrated for brain tissue in [23] by the same authors of this study. We hypothesized that two phenomena drive the malignant evolution of the disease: hypoxia and cell-ECM signaling. To assess patient-specific measurement, we adopted the imaging-informed framework. The same clinical imaging dataset (MRI methods and segmentation), at two time points, was used to initialize and calibrate the parameters. The first point was the pre-operative checkpoint and the second was performed after 6 cycles of concomitant radio-chemotherapy. A last subset of parameters, which do not belong to brain tissue material properties and can not be assess by imaging, was fixed by clinical and experimental literature. After calibration, we obtained a simulated tumor with a 3.5% error in volume, comparatively to the patient tumor, and which overlaps 81.8% of the patient tumor.

Qualitatively, we showed that the mechanical inhibition of the tumor growth describe well the stable zones of the patient tumor, but are not always relevant in the progression zones of the patient tumor. Indeed, few zones of progression (see Figure 4B3) in the patient data undergo this pressure in the simulation, and this pressure could be impede the progression in the simulation. Finally, a large progression zone (see Figure 4C3) in the patient data is not subjected to the inhibiting pressure threshold p_{crit} in the simulation and, however, show no progression in the simulation. We note that the calibrated parameter $p_{\mathrm{crit}} = 1.4 \, \mathrm{kPa}$ is lower than the only other example, to our knowledge, in the literature, estimated with the GBM cell line A172 by Kalli *et al.* in [58]. We also showed that our modeling of the GBMwt phenotype switch behave accordingly to the experimental findings. It has been shown that an ECM stiffer than usual brain ECM provokes GBM cells proliferation *and* migration [59]. The same phenomena are reported under compressive stress and hypoxic environment [22]. ECM stiffness and compressive stress are linked, as in a proliferative environment, a stiffer matrix will allow a higher internal stress. An inhibiting pressure threshold and an internal stress, resulting of a stiffened ECM,
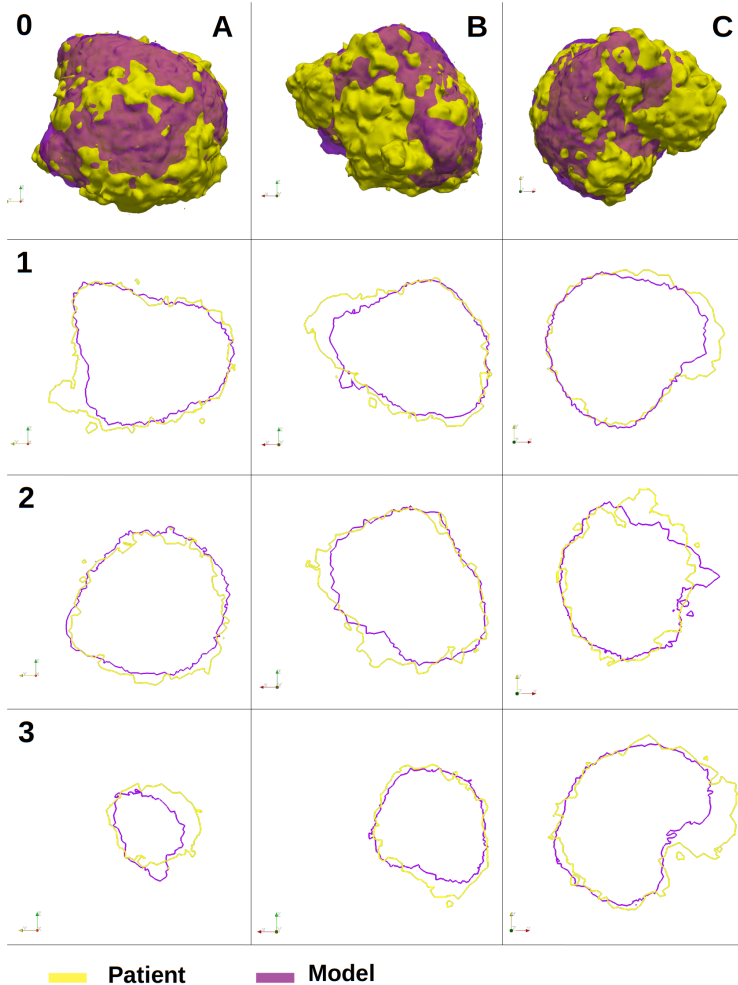
Figure 5: **Overlapping of numerical results and patient segmentation at $T + 3$ months.** **A** Sagittal view (along x axis). **B** Coronal view (along y axis). **C** Axial view (along z axis). **0** 3D isoline, $\mathrm{Vol}_{TC} = 0.001$, numerical (purple) ; patient (yellow). **1** $x = -0.0180$, $y = -0.0104$, $z = 0.0416$. **2A** $x = -0.0390$; **2B** $y = 0.0058$; **2C** $z = 0.0248$. **3A** $x = 0.0054$; **3B** $y = -0.0291$; **3C** $z = 0.0533$. $J_{\mathrm{over}} = 0.188$

which provokes a malignant phenotype switch are not contradictory. They suggest it exists a window of mechanical signaling where GBM can dramatically evolved. Before the phenotype switch, GBMwt cells produce a stiffer, cross-linked, ECM. This stiffening, accompanied by the GBMwt proliferation, increase the internal pressure. If the pressure undergone by the GBMwt reaches the threshold p_{idh} and the level of oxygen is pathologically low (threshold ω_{crit}), the affected GBMwt cells change their phenotype. They become much more mobile, which is translated at the macroscale by a reduction of the dynamic viscosity of three orders and they acquire an anaerobic metabolism pathway, which allow for escaping an hypoxic environment by metabolising lipids [60].

However, this study apply to only one patient, and a third time point of patient data after the temozolomide maintenance, which was necessary to validate the parameters and calibrate the treatment response, was not available. Therefore, we only aim to a proposition of modeling of this disease, *via* porous mechanics and mechano-biology. Several leads are available to improve this proposition. The parameters specific to the patient's cell line could be pre-calibrated by exploiting the *in vitro* results of [58]. A study was already done on encapsulation in alginate of colon carcinoma spheroids, and the parameters were validated with a multiphase poromechanical model in [18] by the same authors of this study. Additionally, a porous model is well adapted to simulate the activity of matrix metalloproteases, the enzymes produced by tumor cells which degrade the extra-cellular matrix. This could a lead to assess the invasive zones of the patient tumor for which our model is still blind. Finally, the addition of diffusion tensor imaging method, which allow for retrieving the white matter fiber direction, would grant the access to an anisotropic permeability. This imaging method is currently a promising lead for modeling the heterogeneous progression of glioblastoma [61, 62].
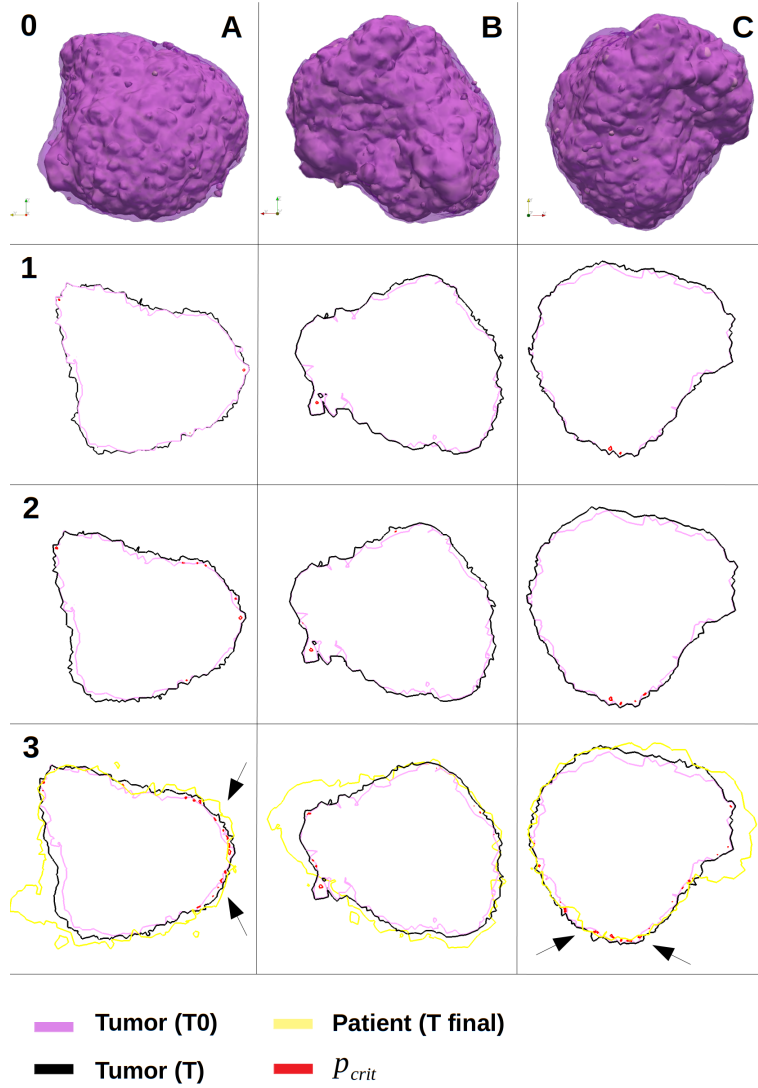
Figure 6: **Influence of mechanical inhibition of tumor growth. A** Sagittal view (along x axis). **B** Coronal view (along y axis). **C** Axial view (along z axis).**0** 3D isoline, $\text{Vol}_{TC} = 0.001$, numerical at T_0 (purple) ; numerical at $T + 63\,\text{days}$ (purple transparent); isoline of inhibiting pressure p_{crit} (red). **1**, **2**, **3** slices centered at $x = -0.0180$, $y = -0.0104$, $z = 0.0416$. **1** numerical at T_0 (purple); numerical at $T + 21\,\text{days}$ (black). **2** numerical at $T + 42\,\text{days}$ (black) after 3 cycles of RT-TMZ treatment. **3** numerical at $T + 63\,\text{days}$ (black) after 6 cycles of RT-TMZ treatment; black arrows indicate relevant area where the inhibiting pressure p_{crit} is reach. Other isoline could impede the GBMwt growth in invasive zones present in patient data.

This study is only a first step of the inclusion of poromechanics in image-informed glioblastoma models, we hope the community will find it inspiring.
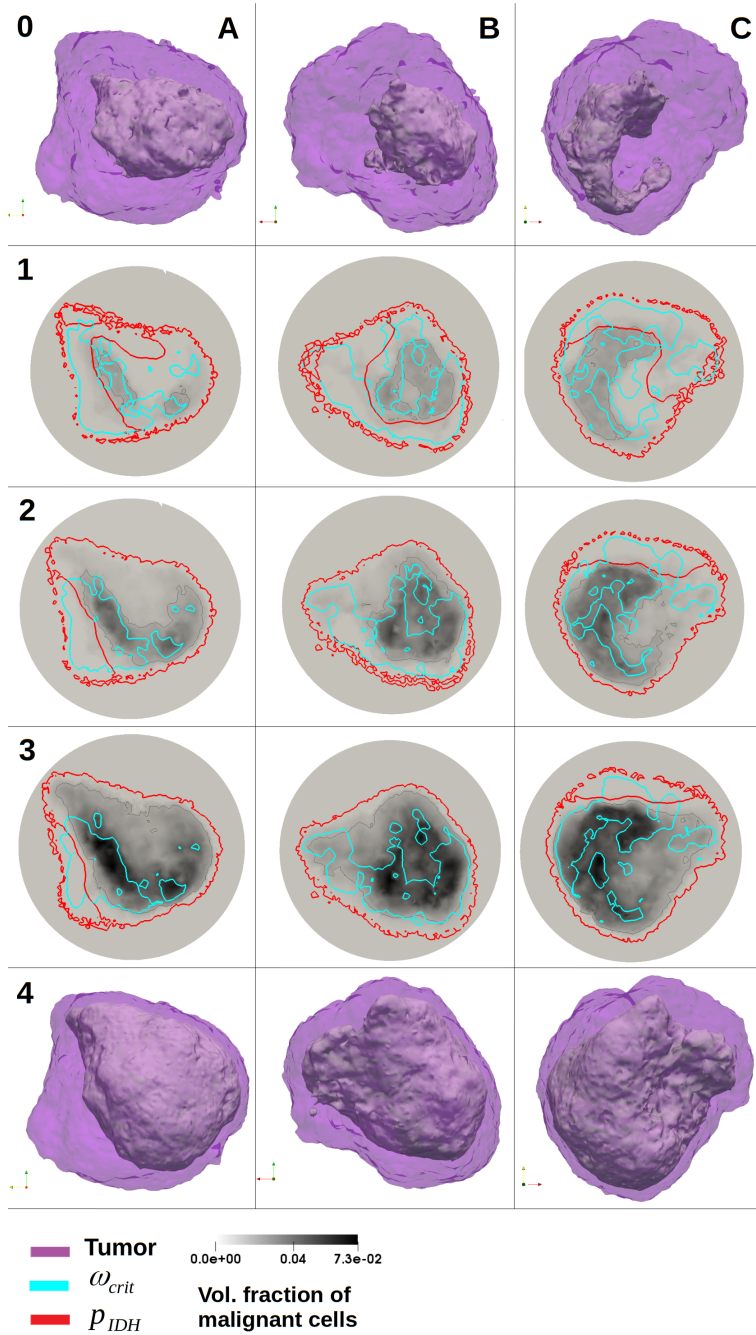
Acknowledgments

Figure 7: **Influence of malignant phenotype in tumor growth and treatment response.** **A** Sagittal view (along x axis). **B** Coronal view (along y axis). **C** Axial view (along z axis). **0** 3D isoline at T_0, $\mathrm{Vol}_{TC} = 0.001$ (purple), $\mathrm{Vol}_{mal} = 0.001$ (grey). **1**, **2**, **3** slices centered at $x = -0.0180$, $y = -0.0104$, $z = 0.0416$; volume fraction of malignant GBMwt cells (grey level); isoline of phenotype switch pressure p_{idh} (red); isoline of hypoxia threshold ω_{crit} (cyan). **1** $T+21$ days; **2** $T+42$ days at 3 cycles of RT-TMZ treatment; **3** $T+63$ days at 6 cycles of RT-TMZ treatment. **4** 3D isoline at $T+63$ days, $\mathrm{Vol}_{TC} = 0.001$ (purple), $\mathrm{Vol}_{mal} = 0.001$ (grey). The malignant phenotype switch is dependent of two concomitant phenomena: a high mechanical pressure inside a hypoxic environment. After their phenotype switch, the malignant GBMwt cells Vol_{mal} progress in the opposite direction of hypoxic zones. During the 6 cycles of RT-TMZ treatment, the volume and the density of Vol_{mal} almost double.

21

A Solution's sensitivity on the ROI size

Dirichlet conditions are prescribed at the ROI boundary:

- No displacement

- Fixed pressure

- Fixed oxygen level

- No necrosis

The sensitivity of these boundary conditions is evaluated on tumor evolution. We compare the capillary pressure of the tumor phase p^{th} at each voxel of the domains with four margin sizes: 1.52 ± 0.2cm, 1.77 ± 0.3cm, 2.27 ± 0.3cm, 2.45 ± 0.4cm, denoted margin 1, 2, 3 and 4 respectively. These margins defined 4 computational domains $\Omega_i \in [1,4]$ respectively. These domains contain 392 k, 425 k, 465 k and 511 k tetrahedrons respectively. The larger domain Ω_4 is used as the reference. The RMSE, without normalization, is computed as follows:

$$RMSE(p_i^{th}, p_4^{th}, n) = \sqrt{\frac{1}{n} \sum_{k=1}^{n} \left(p_4^{th}(k) - p_i^{th}(k) \right)^2} \qquad n = \mathrm{Card}(\Omega_i) \quad i \in [1,3] \tag{53}$$

The results of the model are evaluated by the tumor cells volume fraction Vol_{TC} and its threshold is $\mathrm{Vol}_{TC} \geq 10^{-3}$. This value corresponds, *via* l'Eq.29 for S^t and the range of value for the porosity, to 1.4 ± 0.1 Pa. Therefore, we consider that the RMSE in *textPa* presented Eq.53 above 1.4 Pa is not negligible. At day 18, the RMSE between margins 1 and 4 reaches 0.4 Pa, the RMSE between margins 2 and 4 reaches 0.17 Pa and the RMSE between margins 3 and 4 reaches 0.1 Pa. Hence, we consider that the boundary conditions of the domain Ω_3 have a negligible influence on the numerical solution.
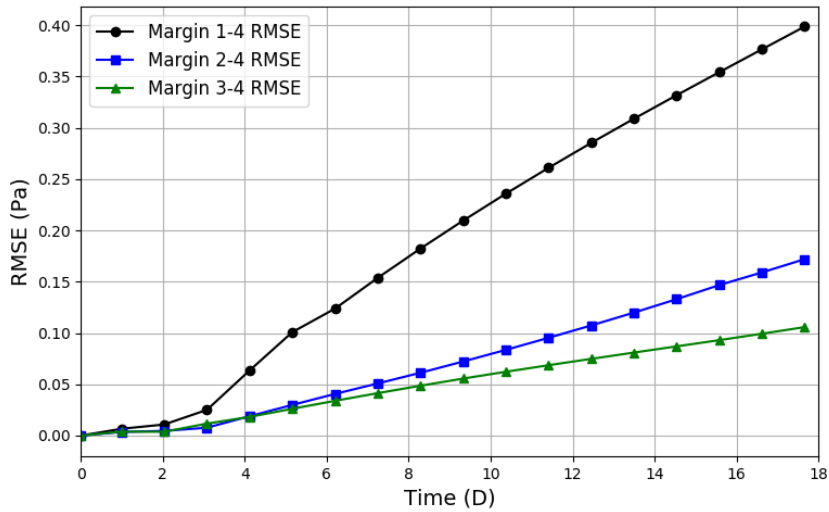

Figure 8: **Influence of the Dirichlet boundary distance on the tumor evolution.** RMSE between margins 1 and 4 (black line, circle marker); RMSE between margins 3 and 4 (green line, triangle marker). To be acceptable, the RMSE should remain below 1.4 Pa. At day 18, the RMSE between margins 1 and 4 reaches 0.4 Pa, the RMSE between margins 2 and 4 reaches 0.17 Pa, and the RMSE between margins 3 and 4 reaches 0.1 Pa

References

[1] Hyuna Sung, Jacques Ferlay, Rebecca L. Siegel, Mathieu Laversanne, Isabelle Soerjomataram, Ahmedin Jemal, and Freddie Bray. Global cancer statistics 2020: Globocan estimates of incidence and mortality worldwide for 36 cancers in 185 countries. *CA: A Cancer Journal for Clinicians*.

[2] Aaron C. Tan, David M. Ashley, Giselle Y. López, Michael Malinzak, Henry S. Friedman, and Mustafa Khasraw. Management of glioblastoma: State of the art and future directions. *CA: A Cancer Journal for Clinicians*, 70(4):299–312, 2020.

[3] DN Louis, A Perry, and G Reifenberger. The 2016 world health organization classification of tumors of the central nervous system: a summary. *Acta Neuropathol.*, 131:803–820, 2016.

[4] Jacopo Falco, Abramo Agosti, Ignazio G. Vetrano, Alberto Bizzi, Francesco Restelli, Morgan Broggi, Marco Schiariti, Francesco DiMeco, Paolo Ferroli, Pasquale Ciarletta, and Francesco Acerbi. In silico mathematical modelling for glioblastoma: A critical review and a patient-specific case. *Journal of Clinical Medicine*, 10(10), 2021.

[5] K R Swanson, E C Alvord, and J D Murray. Virtual brain tumours (gliomas) enhance the reality of medical imaging and highlight inadequacies of current therapy. *British Journal of Cancer*, 86:14–18, 2002.

[6] K. R. Swanson, R. C. Rostomily, and E. C. Alvord. A mathematical modelling tool for predicting survival of individual patients following resection of glioblastoma: A proof of principle. *Br. J. Cancer*, 98(1):113–119, 2008.

[7] Maxwell Lewis Neal, Andrew D. Trister, Tyler Cloke, Rita Sodt, Sunyoung Ahn, Anne L. Baldock, Carly A. Bridge, Albert Lai, Timothy F. Cloughesy, Maciej M. Mrugala, Jason K. Rockhill, Russell C. Rockne, and Kristin R. Swanson. Discriminating survival outcomes in patients with glioblastoma using a simulation-based, patient-specific response metric. *PLoS ONE*, 8(1):e51951, 2013.

[8] Russell C Rockne, Andrew D Trister, Joshua Jacobs, Andrea J Hawkins-Daarud, Maxwell L Neal, Kristi Hendrickson, Maciej M Mrugala, Jason K Rockhill, Paul Kinahan, Kenneth A Krohn, and Kristin R Swanson. A patient-specific computational model of hypoxia-modulated radiation resistance in glioblastoma using (18)F-FMISO-PET. *J. R. Soc. Interface*, 12(103):20141174, 2015.

[9] Thomas E. Yankeelov, Nkiruka Atuegwu, David Hormuth, Jared A. Weis, Stephanie L. Barnes, Michael I. Miga, Erin C. Rericha, and Vito Quaranta. Clinically relevant modeling of tumor growth and treatment response. *Science Translational Medicine*, 5(187), 2013.

[10] Angela M. Jarrett, David A. Hormuth, Chengyue Wu, Anum S. Kazerouni, David A. Ekrut, John Virostko, Anna G. Sorace, Julie C. DiCarlo, Jeanne Kowalski, Debra Patt, Boone Goodgame, Sarah Avery, and Thomas E. Yankeelov. Evaluating patient-specific neoadjuvant regimens for breast cancer via a mathematical model constrained by quantitative magnetic resonance imaging data. *Neoplasia*, 22(12):820–830, 2020.

[11] Guillermo Lorenzo, Thomas J. R. Hughes, Pablo Dominguez-Frojan, Alessandro Reali, and Hector Gomez. Computer simulations suggest that prostate enlargement due to benign prostatic hyperplasia mechanically impedes prostate cancer growth. *Proceedings of the National Academy of Sciences*, 116(4):1152–1161, 2019.

[12] A. Agosti, P. Ciarletta, H. Garcke, and M. Hinze. Learning patient-specific parameters for a diffuse interface glioblastoma model from neuroimaging data. *Mathematical Methods in the Applied Sciences*, 43(15):8945–8979, 2020.

[13] David A Hormuth, Karine A Al Feghali, Andrew M Elliott, Thomas E Yankeelov, and Caroline Chung. Image-based personalization of computational models for predicting response of high-grade glioma to chemoradiation. *Sci. Rep.*, 11:8520, 2021.

[14] Jana Lipková, Panagiotis Angelikopoulos, Stephen Wu, Esther Alberts, Benedikt Wiestler, Christian Diehl, Christine Preibisch, Thomas Pyka, Stephanie E. Combs, Panagiotis Hadjidoukas, Koen Van Leemput, Petros Koumoutsakos, John Lowengrub, and Bjoern Menze. Personalized radiotherapy design for glioblastoma: Integrating mathematical tumor models, multimodal scans, and Bayesian inference. *IEEE Transactions on Medical Imaging*, 38(8):1875–1884, 2019.

[15] Stelios Angeli, Kyrre E. Emblem, Paulina Due-Tonnessen, and Triantafyllos Stylianopoulos. Towards patient-specific modeling of brain tumor growth and formation of secondary nodes guided by DTI-MRI. *NeuroImage: Clinical*, 20:664–673, 2018.

[16] Andreas Mang, Spyridon Bakas, Shashank Subramanian, Christos Davatzikos, and George Biros. Integrated biophysical modeling and image analysis: application to neuro-oncology. *Annu. Rev. Biomed. Eng.*, 22:309–341, 2020.

[17] G Sciumè, R Santagiuliana, M Ferrari, P Decuzzi, and B A Schrefler. A tumor growth model with deformable ecm. *Physical biology*, 11(6), 2014.

[18] Stéphane Urcun, Pierre-Yves Rohan, Wafa Skalli, Pierre Nassoy, Stéphane P. A. Bordas, and Giuseppe Sciumè. Digital twinning of cellular capsule technology: Emerging outcomes from the perspective of porous media mechanics. *PLOS ONE*, 16(7):1–30, 07 2021.

[19] Hermann B. Frieboes, Bryan R. Smith, Yao-Li Chuang, Ken Ito, Allison M. Roettgers, Sanjiv S. Gambhir, and Vittorio Cristini. An integrated computational/experimental model of lymphoma growth. *PLOS Computational Biology*, 9(3):1–13, 03 2013.

[20] Wolfgang Ehlers and Arndt Wagner. Multi-component modelling of human brain tissue: a contribution to the constitutive and computational description of deformation, flow and diffusion processes with application to the invasive drug-delivery problem. *Computer Methods in Biomechanics and Biomedical Engineering*, 18(8):861–879, 2015. PMID: 24261340.

[21] B Muz, P de la Puente, F Azab, and AK Azab. The role of hypoxia in cancer progression, angiogenesis, metastasis, and resistance to therapy. *Hypoxia (Auckl)*, 3:83–92, 2015.

[22] J. Matthew Barnes, Laralynne Przybyla, and Valerie M. Weaver. Tissue mechanics regulate brain development, homeostasis and disease. *Journal of Cell Science*, 130(1):71–82, 2017.

[23] Stéphane Urcun, Pierre-Yves Rohan, Giuseppe Sciumè, and Stéphane P.A. Bordas. Cortex tissue relaxation and slow to medium load rates dependency can be captured by a two-phase flow poroelastic model. *Journal of the Mechanical Behavior of Biomedical Materials*, 126:104952, 2022.

[24] G. Franceschini, D. Bigoni, P. Regitnig, and G.A. Holzapfel. Brain tissue deforms similarly to filled elastomers and follows consolidation theory. *Journal of the Mechanics and Physics of Solids*, 54(12):2592–2620, 2006.

[25] Silvia Budday, Richard Nay, Rijk de Rooij, Paul Steinmann, Thomas Wyrobek, Timothy C Ovaert, and Ellen Kuhl. Mechanical properties of gray and white matter brain tissue by indentation. *Journal of the mechanical behavior of biomedical materials*, 46:318—330, June 2015.

[26] Pietro Mascheroni, Cinzia Stigliano, Melania Carfagna, Daniela P. Boso, Luigi Preziosi, Paolo Decuzzi, and Bernhard A. Schrefler. Predicting the growth of glioblastoma multiforme spheroids using a multiphase porous media model. *Biomechanics and Modeling in Mechanobiology*, 15(1):1215–1228, 2016.

[27] Raffaella Santagiuliana, Miljan Milosevic, Bogdan Milicevic, Giuseppe Sciumè, Vladimir Simic, Arturas Ziemys, Milos Kojic, and Bernhard A Schrefler. Coupling tumor growth and bio distribution models. *Biomedical microdevices*, 21, 2019.

[28] Hui Zong, Luis F. Parada, and Suzanne J. Baker. Cell of origin for malignant gliomas and its implication in therapeutic development. *Cold Spring Harbor Perspectives in Biology*, 7(5), 2015.

[29] Roger Stupp, Warren P. Mason, Martin J. van den Bent, Michael Weller, Barbara Fisher, Martin J.B. Taphoorn, Karl Belanger, Alba A. Brandes, Christine Marosi, Ulrich Bogdahn, Jürgen Curschmann, Robert C. Janzer, Samuel K. Ludwin, Thierry Gorlia, Anouk Allgeier, Denis Lacombe, J. Gregory Cairncross, Elizabeth Eisenhauer, and René O. Mirimanoff. Radiotherapy plus concomitant and adjuvant temozolomide for glioblastoma. *New England Journal of Medicine*, 352(10):987–996, 2005. PMID: 15758009.

[30] Juan Huang, Jialong Yu, Lin Tu, Nanqu Huang, Hang Li, and Yong Luo. Isocitrate dehydrogenase mutations in glioma: From basic discovery to therapeutics development. *Frontiers in Oncology*, 9:506, 2019.

[31] Monika E. Hegi, Annie-Claire Diserens, Thierry Gorlia, Marie-France Hamou, Nicolas de Tribolet, Michael Weller, Johan M. Kros, Johannes A. Hainfellner, Warren Mason, Luigi Mariani, Jacoline E.C. Bromberg, Peter Hau, René O. Mirimanoff, J. Gregory Cairncross, Robert C. Janzer, and Roger Stupp. Mgmt gene silencing and benefit from temozolomide in glioblastoma. *New England Journal of Medicine*, 352(10):997–1003, 2005. PMID: 15758010.

[32] Arnab Chakravarti, Michael G. Erkkinen, Ulf Nestler, Roger Stupp, Minesh Mehta, Ken Aldape, Mark R. Gilbert, Peter McL. Black, and Jay S. Loeffler. Temozolomide-mediated radiation enhancement in glioblastoma: A report on underlying mechanisms. *Clinical Cancer Research*, 12(15):4738–4746, 2006.

[33] William G. Gray and Cass T. Miller. *Introduction to the Thermodynamically Constrained Averaging Theory for Porous Medium Systems*. Springer, 2014.

[34] Katie Bentley and Shilpa Chakravartula. The temporal basis of angiogenesis. *Philosophical Transactions of the Royal Society B: Biological Sciences*, 372(1720):20150522, 2017.

[35] Arin Nam, Atish Mohanty, Supriyo Bhattacharya, Sourabh Kotnala, Srisairam Achuthan, Kishore Hari, and Anusha Nathan. Suppressing chemoresistance in lung cancer via dynamic phenotypic switching and intermittent therapy. *bioRxiv*, 2020.

[36] Giuseppe Sciumè, Mauro Ferrari, and Bernhard A. Schrefler. Saturation–pressure relationships for two- and three-phase flow analogies for soft matter. *Mechanics Research Communications*, 62:132 – 137, 2014.

[37] G Sciumè, W G Gray, F Hussain, M Ferrari, P Decuzzi, and B A Schrefler. Three phase flow dynamics in tumor growth. *Computational Mechanics*, 53(3):465–484, 2014.

[38] Wei Xing, Min Yin, Qing Lv, Yang Hu, Changpeng Liu, and Jiujun Zhang. 1 - oxygen solubility, diffusion coefficient, and solution viscosity. In Wei Xing, Geping Yin, and Jiujun Zhang, editors, *Rotating Electrode Methods and Oxygen Reduction Electrocatalysts*, pages 1–31. Elsevier, Amsterdam, 2014.

[39] Gabriel Alzial, Ophelie Renoult, François Paris, Catherine Gratas, Anne Clavreul, and Claire Pecqueur. Wild-type isocitrate dehydrogenase under the spotlight in glioblastoma. *Oncogene*, 2021.

[40] Esteban Ortiz-Prado, Jeff F Dunn, Jorge Vasconez, Diana Castillo, Ginés Viscor, Frederick Warner, and Steven W Zucker. Partial pressure of oxygen in the human body: a general review. *American journal of blood research*, 9(1):1–14, 2019.

[41] Nadeem Khan, Benjamin B. Williams, Huagang Hou, Hongbin Li, and Harold M. Swartz. Repetitive tissue po2 measurements by electron paramagnetic resonance oximetry: Current status and future potential for experimental and clinical studies. *Antioxidants & Redox Signaling*, 9(8):1169–1182, 2007. PMID: 17536960.

[42] Konstantinos Kamnitsas, Enzo Ferrante, Sarah Parisot, Christian Ledig, Aditya V. Nori, Antonio Criminisi, Daniel Rueckert, and Ben Glocker. Deepmedic for brain tumor segmentation. In Alessandro Crimi, Bjoern Menze, Oskar Maier, Mauricio Reyes, Stefan Winzeck, and Heinz Handels, editors, *Brainlesion: Glioma, Multiple Sclerosis, Stroke and Traumatic Brain Injuries*, pages 138–149, Cham, 2016. Springer International Publishing.

[43] Y. Zhang, M. Brady, and S. Smith. Segmentation of brain mr images through a hidden markov random field model and the expectation-maximization algorithm. *IEEE Transactions on Medical Imaging*, 20(1):45–57, 2001.

[44] Fulvio Zaccagna, Frank Riemer, Andrew N. Priest, Mary A. McLean, Kieren Allinson, James T. Grist, Carmen Dragos, Tomasz Matys, Jonathan H. Gillard, Colin Watts, Stephen J. Price, Martin J. Graves, and Ferdia A. Gallagher. Non-invasive assessment of glioma microstructure using verdict mri: correlation with histology. *European Radiology*, 29:5559–5566, 2019.

[45] Asad Jamal, Maria Teresa Mongelli, Marco Vidotto, Michael Madekurozwa, Andrea Bernardini, Darryl R. Overby, Elena De Momi, Ferdinando Rodriguez y Baena, Joseph M. Sherwood, and Daniele Dini. Infusion mechanisms in brain white matter and their dependence on microstructure: An experimental study of hydraulic permeability. *IEEE Transactions on Biomedical Engineering*, 68(4):1229–1237, 2021.

[46] Judah Folkman. Tumor angiogenesis: Therapeutic implications. *New England Journal of Medicine*, 285(21):1182–1186, 1971. PMID: 4938153.

[47] Yiming Lei, Hongbin Han, Fan Yuan, Aqeel Javeed, and Yong Zhao. The brain interstitial system: Anatomy, modeling, in vivo measurement, and applications. *Progress in Neurobiology*, 157:230 – 246, 2017. New Perspectives on Healthy Aging.

[48] Gaspar J. Kitange, Brett L. Carlson, Mark A. Schroeder, Patrick T. Grogan, Jeff D. Lamont, Paul A. Decker, Wenting Wu, C. David James, and Jann N. Sarkaria. Induction of MGMT expression is associated with temozolomide resistance in glioblastoma xenografts. *Neuro-Oncology*, 11(3):281–291, 06 2009.

[49] Martin Alnæs, Jan Blechta, Johan Hake, August Johansson, Benjamin Kehlet, Anders Logg, Chris Richardson, Johannes Ring, Marie Rognes, and Garth Wells. The fenics project version 1.5. *Archive of Numerical Software*, 3(100), 2015.

[50] Saumik Dana and Mary F Wheeler. Design of convergence criterion for fixed stress split iterative scheme for small strain anisotropic poroelastoplasticity coupled with single phase flow, 2021.

[51] Sébastien Benzekry, Clare Lamont, Afshin Beheshti, Amanda Tracz, John M. L. Ebos, Lynn Hlatky, and Philip Hahnfeldt. Classical mathematical models for description and prediction of experimental tumor growth. *PLOS Computational Biology*, 10(8):1–19, 08 2014.

[52] Gabriel Helmlinger, Paolo A. Netti, Hera C. Lichtenbeld, Robert J. Melder, and Rakesh K. Jain. Solid stress inhibits the growth of multicellular tumor spheroids. *Nature Biotechnology*, 15(21):778–783, 1997.

[53] Gang Cheng, Janet Tse, Rakesh K. Jain, and Lance L. Munn. Micro-environmental mechanical stress controls tumor spheroid size and morphology by suppressing proliferation and inducing apoptosis in cancer cells. *PLOS ONE*, 4(2):1–11, 02 2009.

[54] Kévin Alessandri, Bibhu Ranjan Sarangi, Vasily Valériévitch Gurchenkov, Bidisha Sinha, Tobias Reinhold Kießling, and Luc *et al.* Fetler. Cellular capsules as a tool for multicellular spheroid production and for investigating the mechanics of tumor progression in vitro. *Proceedings of the National Academy of Sciences*, 110(37):14843–14848, 2013.

[55] Rémy Brossel, Alexandre Yahi, Stéphane David, Laura Moreno Velasquez, and Jean-Marc Guinebretière. Mechanical signals inhibit growth of a grafted tumor in vivo: Proof of concept. *PLOS ONE*, 11:1–17, 04 2016.

[56] Rakesh K. Jain, John D. Martin, and Triantafyllos Stylianopoulos. The role of mechanical forces in tumor growth and therapy. *Annual Review of Biomedical Engineering*, 16(1):321–346, 2014.

[57] Hadi T. Nia, Lance L. Munn, and Rakesh K. Jain. Physical traits of cancer. *Science*, 370(6516), 2020.

[58] Maria Kalli, Chrysovalantis Voutouri, Angeliki Minia, Vaia Pliaka, Christos Fotis, Leonidas G. Alexopoulos, and Triantafyllos Stylianopoulos. Mechanical compression regulates brain cancer cell migration through mek1/erk1 pathway activation and gdf15 expression. *Frontiers in Oncology*, 9:992, 2019.

[59] Theresa A. Ulrich, Elena M. de Juan Pardo, and Sanjay Kumar. The mechanical rigidity of the extracellular matrix regulates the structure, motility, and proliferation of glioma cells. *Cancer Research*, 69(10):4167–4174, 2009.

[60] Ioanna Prionisti, Léo H. Bühler, Paul R. Walker, and Renaud B. Jolivet. Harnessing microglia and macrophages for the treatment of glioblastoma. *Frontiers in Pharmacology*, 10:506, 2019.

[61] K.J. Painter and T. Hillen. Mathematical modelling of glioma growth: The use of diffusion tensor imaging (dti) data to predict the anisotropic pathways of cancer invasion. *Journal of Theoretical Biology*, 323:25–39, 2013.

[62] Marie-Christin Metz, Miguel Molina-Romero, Jana Lipkova, Jens Gempt, Friederike Liesche-Starnecker, Paul Eichinger, Lioba Grundl, Bjoern Menze, Stephanie E. Combs, Claus Zimmer, and Benedikt Wiestler. Predicting glioblastoma recurrence from preoperative mr scans using fractional-anisotropy maps with free-water suppression. *Cancers*, 12(3), 2020.

[63] S. Varrette, P. Bouvry, H. Cartiaux, and F. Georgatos. Management of an academic hpc cluster: The ul experience. In *Proc. of the 2014 Intl. Conf. on High Performance Computing & Simulation (HPCS 2014)*, pages 959–967, Bologna, Italy, July 2014. IEEE.